Microphysical evolution in mixed-phase mid-latitude marine cold-air outbreaks

Seethala Chellappan,[1] Paquita Zuidema,[1] Simon Kirschler,[2] Christiane Voigt,[2] Brian Cairns,[3] Ewan C. Crosbie,[4] Richard Ferrare,[5] Johnathan Hair,[5] David Painemal,[4] Taylor Shingler,[5] Michael Shook,[5] Kenneth L. Thornhill,[5] Florian Tornow,[3] and Armin Sorooshian[6]

[1] *Department of Atmospheric Sciences, Rosenstiel School, University of Miami, Miami, Florida, USA*

[2] *Institut für Physik der Atmosphäre, Deutsches Zentrum für Luft- und Raumfahrt (DLR), Oberpfaffenhofen, Germany*

[3] *Goddard Institute for Space Studies, New York City, New York, USA*

[4] *AMA, Hampton, Virginia, USA*

[5] *NASA Langley Research Center, Hampton, Virginia, USA*

[6] *Department of Chemical and Environmental Engineering, University of Arizona, Tucson, Arizona, USA*

This is a non-peer-reviewed prepring submitted to EarthArXiv, under consideration for publication within the AMS Journal of Atmospheric Sciences

Corresponding author: Paquita Zuidema, pzuidema@miami.edu and Seethala Chellappan, seethala.chellappan@miami.edu

ABSTRACT: Five cold-air outbreaks are investigated with aircraft offshore of continental northeast American. Flight paths aligned with the cloud-layer flow span cloud-top temperatures of -5 to -12 °C, *in situ* liquid water paths of up to 600 g m^{-2}, while *in situ* cloud droplet number concentrations exceeding 500 cm^{-3} maintain effective radii below 10 μm. Ice is usually present at cloud initiation. Further downstream, ice particle number concentrations (N_i) of 0.1-2.5 L^{-1} indicate secondary ice production. This is enhanced near cloud top, consistent with collisional breakup of graupel and vapor-grown ice particles, and near cloud base, where ice aggregates near 0 °C. Rime-splintering is clearly evident. The highest ice water contents coincide with temperatures favoring dendritic growth. Warmer clouds and weaker surface fluxes correlate to fewer ice particles. Buoyancy fluxes reach 400-600 W m^{-2} near the Gulf Stream's western edge, with updrafts reaching five m s^{-1} supporting closely-spaced convective cells. Upper-level detrainment maintains a high overall cloud fraction despite decoupled boundary layer vertical structures. The near-surface liquid rainfall rates of three more intense cold-air outbreaks are a maximum near the Gulf Stream's eastern edge, just before the clouds transition to more open-celled structures, and correspond to higher cloud liquid water paths. The milder two cold-air outbreaks transition to lower-albedo cumulus through cloud thinning.

SIGNIFICANCE STATEMENT: Cold-air outbreaks off of the eastern US seaboard provide dramatic visual examples of cloud transitions from overcast, high-albedo convective clouds to more broken cloud fields. We use data from the recent NASA ACTIVATE (Aerosol Cloud meTeorology Interactions oVer the western ATlantic Experiment) aircraft campaign to examine the microphysics and environmental context of five such outbreaks. We find the clouds are not ice-deprived, but updrafts still supply significant liquid water. Cloud transitions are encouraged through precipitation for the deeper clouds, and, boundary layer warming and drying through entrainment for the thinner clouds. These observations help constrain further modeling studies examining how cloud processes affect the cloud reflectivity, impacting climate prediction, and surface rainfall rates, important for weather forecasting.

1. Introduction

Cold-air outbreaks (CAOs) off of the eastern US seaboard provide dramatic visual examples of cloud morphological transitions, including from closed-cell to more open-celled circulations. Space-based lidar and radar indicate super-cooled liquid clouds overlying melting snow are common over the northwest Atlantic, with a significant latitudinal gradient in snow fraction (Field and Heymsfield 2015; Mülmenstadt et al. 2015; Matus and L'Ecuyer 2017). Model representations of the partitioning between liquid and ice have significant ramifications for the cloud albedo over the southern oceans, with too much ice generating too-dim clouds in CMIP5 models, and too much liquid generating too-bright clouds in CMIP6 models (Zelinka et al. 2020). A warmer climate may encourage more liquid clouds at the expense of ice clouds (the cloud phase feedback) (Mitchell et al. 1989; Frey et al. 2018), in which the smaller size of liquid droplets enhances the reflection of sunlight back to space for the same water mass. If this occurs at temperatures below 0 °C, the liquid clouds can become optically thicker as temperatures warm, because more water vapor is available to convert into liquid (the cloud optical depth feedback) (Tan et al. 2016; Terai et al. 2019; Wall et al. 2022; McGraw et al. 2023).

In the high-latitude regions, model solar radiation biases are most pronounced behind the cold fronts of synoptic cyclones, where the total cloud cover is dominated by mixed-phase boundary layer clouds (Bodas-Salcedo et al. 2014). CAOs over open water, fed by strong moisture and heat fluxes, can generate significant precipitation, with implications for shipping and coastal communities. The precipitation-facilitated evolution from closed- to open-celled cloud organization (e.g., Abel et al. 2017) has also remained difficult to model realistically (Field et al. 2017). Interest in improving the understanding, modeling, and prediction of mixed-phase CAOs for both weather and climate has motivated multiple observational campaigns (Wendisch et al. 2019; McFarquhar et al. 2021; Geerts et al. 2022), including over the northwestern Atlantic (Sorooshian et al. 2019).

CAOs in the mid-latitudes, because they occur at warmer temperatures than at higher latitudes, can include both rain and ice. Northwestern Atlantic CAOs first flow over the cold near-shore Labrador current and then the warm Gulf Stream (GS). Large air-sea temperature differences support strong surface turbulent fluxes and rapid cloud deepening, with the strong sea surface temperature (SST) gradients encouraging secondary mesoscale circulations (Liu et al. 2014; Naud et al. 2020), and at times of supporting cyclogenesis (Dirks et al. 1988). Of further note is the outflow of urban anthropogenic pollution encouraging high cloud condensation nuclei (CCN) concentrations and cloud droplet number concentrations (N_d) (Corral et al. 2021; Dadashazar et al. 2021; Kirschler et al. 2022; Gryspeerdt et al. 2022). Elevated N_ds can delay precipitation, discouraging cloud break-up and extending cloud lifetime and coverage in subtropical stratocumulus regions (Christensen et al. 2020). For the rapidly-deepening clouds over the Gulf Stream, entrainment of lower free-tropospheric CCN concentrations will dilute the N_d (Tornow et al. 2022). Combined with high cloud liquid water paths (LWPs), precipitation should decouple the surface from the cloud layer, similar to subtropical stratocumulus and subarctic CAOs (Wood et al. 2011; Abel et al. 2017). Modeling studies suggest glaciation can also hasten cloud transitions (Tornow et al. 2021; Atlas et al. 2022) and, given sufficient ice loading, enhance open-celled organization (Eirund et al. 2019).

Over the southern oceans, ice enhancement through secondary ice production (SIP) is prevalent in mixed-phase clouds (Yang et al. 2021; Järvinen et al. 2022; Atlas et al. 2022), even in thin clouds with relatively warm cloud top temperatures (Zaremba et al. 2021). This suggests an observational link between ice production and transitions in cloud morphology may also exist for northern mid-latitude CAOs. Overall the modeling of primary and secondary ice production remains highly uncertain (Zhao and Liu 2022). The rime-splintering Hallett-Mossop (HM; Hallett and Mossop 1974) mechanism produces secondary ice when droplets of diameter < 13 μm or > 25 μm rime onto large particles, freeze and splinter off as columns (Mossop 1976; Choularton et al. 1980). This mechanism is only active between -3 and -8 °C, and is typically the only SIP process represented in models (e.g., Gettelman et al. 2010; Milbrandt and Morrison 2016). At colder temperatures, colliding ice-ice and ice-graupel particles can breakup (Takahashi et al. 1995). This is more common at temperatures favoring dendritic growth (~ -15°C). Larger drops can also shatter upon freezing (Lawson and Zuidema 2009; Lauber et al. 2018) including through riming (Järvinen et al. 2022). Differences in riming fraction encourage a range of fall velocities that support further collisions (Korolev et al. 2020).

Here we contribute to this growing literature by presenting analysis from the detailed fetch-following characterizations of five winter days with CAOs over the northwest Atlantic, using recent aircraft measurements from the NASA Aerosol Cloud meTeorology Interactions oVer the western ATlantic Experiment (ACTIVATE; Sorooshian et al. 2019). The leading question is whether precipitation is needed to encourage transition to cloud structures with lower cloud fractions and albedos, or, if cloud fractions reduce through dry air entrainment from the free troposphere and/or weakened surface fluxes as the boundary layer deepens. ACTIVATE used a unique campaign strategy of flying two stacked planes to acquire a comprehensive set of measurements of both the environmental context and the embedded clouds. The high and low flying planes, both at speeds of ~ 120 m s^{-1}, aimed to remain within five minutes and six km of each other (Sorooshian et al. 2023). The low flying Langley Falcon HU-25 plane followed a set flight pattern (Fig. 1) to collect *in-situ* cloud and aerosol microphysical measurements. At 8-9 km altitude, an accompanying King Air plane hosted the multiwavelength and depolarization sensitive High-Spectral-Resolution Lidar-2 (HSRL2) measuring aerosol and cloud profiles from which cloud top heights are retrieved, and a Research Scanning Polarimeter (RSP) measuring spectrally-resolved shortwave radiances from which cloud optical properties are retrieved. Dropsondes captured thermodynamic and wind profiles (approximately four per flight). Although the plane speed far exceeds the movement of the air mass, the CAOs are quasi steady-state over the course of the day, as inferred from afternoon characterizations that resemble those from the morning flights. This allows us to comment on the CAO evolution, with the five days drawn from March 2020 and January-March of 2021 providing a reasonable range of synoptic and aerosol conditions. The data from the eight research flights occurring on the five days do not support a comprehensive analysis, but do support a framework in which analysis of further data can be inserted, and allow for non-case-specific findings.

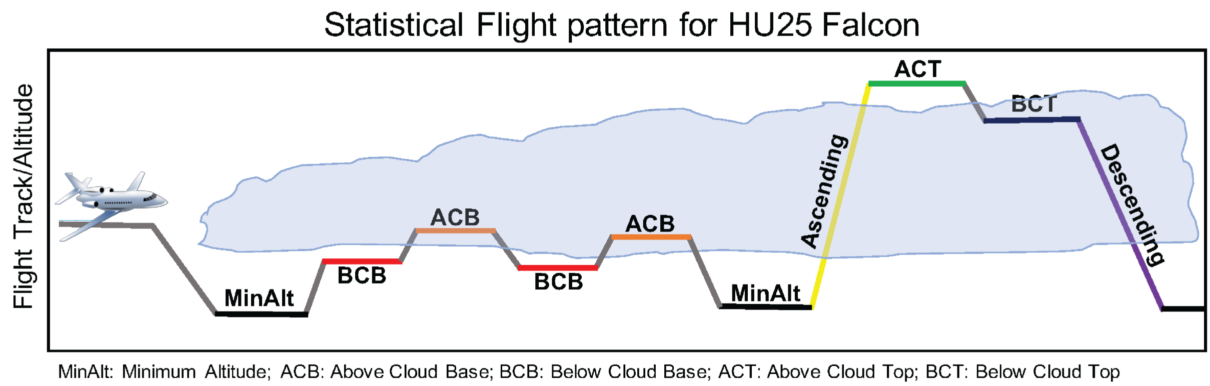

FIG. 1. Typical Falcon flight sampling plan. The same color coding and nomenclature is applied to each flight throughout the manuscript. The minimum altitude (MinAlt) legs occurred at $\sim$ 150 m altitude. BCB=below cloud base, ACB=above cloud base, ACT=above cloud top, and BCT=below cloud top.

The paper is organized as follows: Section 2 outlines the datasets used for this study, Section 3 provides the environmental context, and Section 4 details the flights occurring on the five days. This entails an integrated description of the *in situ* microphysical characteristics with cloud top heights and temperatures, along with reanalysis-derived surface fluxes and measured vertical velocities. After describing each flight, we synthesize their information to examine how ice microphysical quantities and near-surface precipitation depend on cloud-top temperature (T_{ct}), *in situ* temperature and satellite-retrieved liquid water paths (LWPs). Section 5 integrates the information to develop a holistic view of mixed-phase cloud evolution in mid-latitude cold-air outbreaks. An online Supplement provides further supporting documentation.

2. Datasets

Research flights, detailed in Table 1, lasted near four hours, allowing for both morning and afternoon flights on select days.

a. In situ Microphysics

A Fast Cloud Droplet Probe (FCDP) and a Two-Dimensional Stereo (2DS) imager, both developed by the Stratton Park Engineering Company (SPEC) Incorporated and operated by the Deutsches Zentrum für Luft- und Raumfahrt (DLR), and from a Cloud Droplet Probe (CDP) operated by NASA Langley, collected the *in situ* cloud water information. The FCDP measures diameters between 3 to 50 μm at a sampling rate of 25 ns, with a nominal size uncertainty of 10% to 50%, and 3%-10% in N_d (Kirschler et al. 2022, and references therein). The aspect ratio of the FCDP particles is gauged so that mainly spherical FCDP particles contribute to the FCDP-derived bulk quantities. Size bin measurements from the FCDP and 2DS probes overlap between 17.1 to 50 μm, and a combined size distribution spanning 3 to 1465 μm in diameter is constructed, from which the liquid particle number concentrations are identified for three separate radius ranges: cloud (< 20 μm), drizzle (20-54 μm) and rain (> 54 μm) (Kirschler et al. 2023).

The high aerosol loadings advecting off of the populated, industralized, eastern continental seaboard (Dadashazar et al. 2021; Kirschler et al. 2022) challenge the measurements of the cloud droplet number concentrations (N_ds) by both the FCDP and CDP. This is detailed further in the Appendix. We therefore show an average of the FCDP and CDP N_ds in the visualizations of each flight. On the 3 February 2021 flight, the FCDP probe iced, and only corrected (see Appendix) CDP data are shown. In the summary analyses we primarily rely on the FCDP cloud probe data.

The 2DS data provide IWC, N_i, and ice particle habit information. Ice particles are identified through their asphericity, and spherical ice particles (through e.g. riming) can be missed. The 2DS responds to particles of size 5.7 to 1465 μm at a sampling rate of 41 ns, with corrections applied for image distortion, sample area and shattering. The 2DS particle number concentration uncertainty is similar for ice and water (Kirschler et al. 2023). The 2DS detection limit for ice particle concentrations is 10^{-4} cm^{-3} at one Hz sampling, with the analysis limited to non-zero ice particle number concentrations. The optical interaction with small ice columns can generate Poisson focus points in the imagery with the appearance of an 'H' (Vaillant de Guélis et al. 2019).

Individual flight legs last two to four minutes, with most of the analysis relying on leg-means constructed from one-Hz data. Leg-mean N_d are constructed from one-second LWCs exceeding 0.01 g m^{-3} and N_d > 10 cm^{-3}, similar to Kirschler et al. (2023), during Below Cloud Top (BCT), Above Cloud Base (ACB), Below Cloud Base (BCB), and Minimum Altitude (MinAlt, at ~150 m altitude) level legs (Fig. 1). Aircraft ascent rates of ~ eight m s^{-1}, over the four-minute profile legs, imply the plane travels a horizontal distance of ~ 24 km during the ascent. This means horizontal cloud heterogeneities can easily become aliased into the profiles.

b. Remotely-Sensed Variables, Reanalysis, and Other

HSRL2 lidar data can also provide an indication of ice and water phase through the ratio of the volume extinction coefficient to the backscattered intensity, known as the lidar ratio (Hu et al. 2009). The presence of ice will increase the lidar ratio because of a slight difference in the refractive index between ice and water, above that expected for water spheres of the same size. The lidar ratio is invoked at times.

MODIS LWPs are more readily available than those from RSP for the five selected flight days, and can cover a larger spatial domain for each flight. We therefore primarily rely on MODIS LWP to support a comparison across the flights, on the assumption that the retrieval biases are similar across the flights. MODIS values are separated in time by up to two hours from the available profiles. Although the MODIS LWP estimates are likely too low, they do benefit from a compensation between the MODIS cloud optical depth and r_e biases (see fuller assessment within the Appendix).

Global High-Resolution satellite Sea Surface Temperature (GHRSST) contours of 294 K are used to indicate the Gulf Stream (GS). GHRSST's one km spatial resolution is preferred to the coarser 31 km-spatial grid spacing of the ERA5 SSTs, which unrealistically broaden the Gulf Stream (Seethala et al. 2021). Cloud top temperature T_{ct}s are determined from ERA5 temperatures colocated with HSRL-2 cloud-top altitudes. The ERA5 T_{ct} correspond more closely to dropsonde-determined cloud top temperatures than do the MODIS T_{ct}, which can be influenced by surface temperatures (Zuidema et al. 2009). At times, the ERA5 T_{ct} is warmer than the leg-mean temperature of the below-cloud-top (BCT) leg (Fig. S1). Since this is unphysical, the leg-mean *in situ* BCT temperature, when available, is substituted for the ERA5-determined T_{ct}.

ERA5 reanalysis also establishes the intensity of a cold-air outbreak using $M = \theta_{SKT}$ - θ_{850hPa} where θ_{SKT} is the 'skin' SST potential temperature, following Papritz et al. (2015) and Seethala et al. (2021). ERA5 buoyancy fluxes (Q_B) are calculated from the latent (Q_L) and sensible (Q_S) fluxes as $Q_B = Q_S * (1+0.6q_{2m}) + 0.6Q_L\frac{c_p}{L_v}T_{2m}$, where q_{2m} and T_{2m} are the specific humidity and temperature at 2 meters, c_p is the specific heat of air at constant pressure and L_v is the latent heat of vaporization. Lagrangian forward trajectories are constructed based on ERA5 data at 500 m altitude combined with the HYSPLIT air trajectory model, initialized upstream of the flight path. The flight sampling encompasses approximately one day of the trajectory flow.

Table 1. Dates, research flight numbers, plane participation and dropsonde number for each flight day.

date	morning	am dropsondes	afternoon	pm dropsondes
1 March 2020	RF13, both planes	circle of 11	RF14, both planes. no RSP	2 (downwind)
29 January 2021	RF42, King Air (high flying)	2	RF43, Falcon (*in-situ*)	0
3 February 2021	RF44, both planes	5	–	–
5 March 2021	RF49, both planes	5	RF50, both planes	2 (downwind)
8 March 2021	–	–	RF51, both planes	4

Thermodynamic and wind profiles are provided by the National Center for Atmospheric Research's NRD41 dropsondes, described further in Vömel et al. (2023). *In situ* vertical velocities (w), averaged from 20 Hz to a one-second time resolution, are measured with the Turbulent Air Motion Measurement System (TAMMS; Thornhill et al. 2003). No radar was deployed on either plane, nor a Nevzorov total water content cloud probe (useful for constraining bin-resolved liquid water contents), and ice-nucleating particles were not sampled.

3. Overview

The five selected flight days are: 1 March, 2020; 29 January, 2021; 3 February, 2021; 5 March, 2021, and 8 March, 2021 (Fig. 2). Three days contained both morning and afternoon flights (March 1, 2020, 29 January 2021 and 5 March, 2021), with Table 1 listing the number of dropsondes per flight and significant instrument notes. All but the morning flight on 1 March, 2020 followed a flight track approximately aligned with the Lagrangian boundary layer trajectories (Fig. 2, top row). All of the flights cross the cold western edge of the Gulf Stream (Fig. 3b). Maximum MODIS liquid water paths range from 80 g m^{-2} to 250 g m^{-2}. Near-surface ERA5 wind speeds range from 4 to 20 m s $^{-1}$, mostly increasing eastward (Fig. 2, 2nd row; Fig. 3a). The increase is in accord with a surface wind convergence over the warmer waters (Minobe et al. 2008; Small et al. 2008; Plagge et al. 2016). The 750 hPa vertical velocities indicate synoptic subsidence (Fig. 2, third row). As documented in Painemal et al. (2023), the trough and trough-to-ridge portions of mid-latitude cyclones give rise to the coastal northerly winds and subsidence that support CAOs. On 3 February, 2021, the 750 hPa vertical velocities indicate ascent. We show later that 750 hPa is still within the boundary layer on this day. Surface buoyancy fluxes align well with the Gulf Stream boundaries (Fig. 2, bottom row) as does the CAO M index.

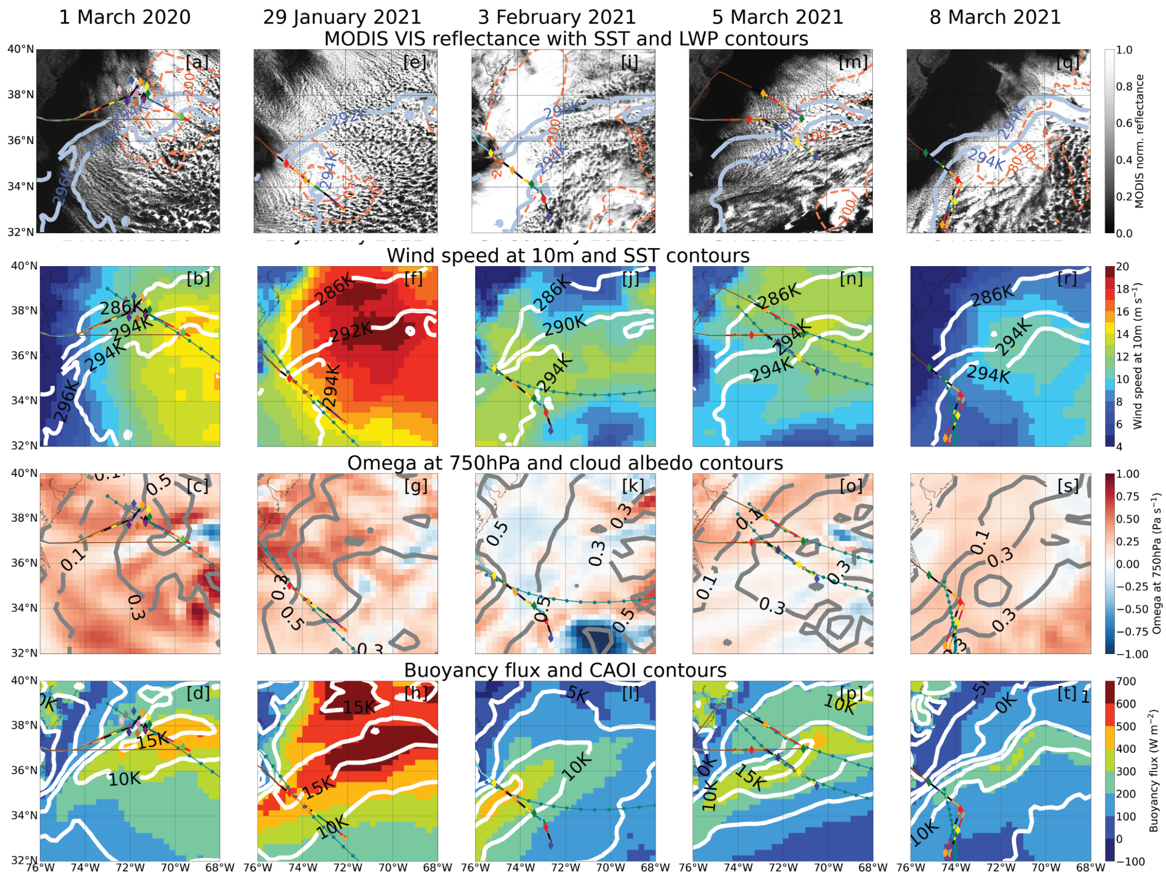

FIG. 2. Top row: MODIS visible imagery, with SST contours at 290K, 292K and/or 294K (dusty blue line), MODIS LWPs at 80,100, 150, 200 and/or 250 g m^{-2} (dashed orange lines), and the Falcon flight tracks, color-coded by altitude and with dropsonde locations indicated (purple diamonds) for a) 1 March 2020, b) 29 January 2021, c) 3 February 2021, d) 5 March 2021 and e) 8 March 2021. 3 February image is from *Terra*, the others from *Aqua*. Second row: ERA5 10m wind speed with SST contours overlaid, Third row: ERA5 vertical velocities at 750 hPa (color) with CERES-MODIS cloud albedo in grey contours; and bottom row: ERA5 buoyancy fluxes (color) overlaid with CAO index (white contours). HYSPLIT trajectories (dark green) initialized at a)-d): 1 March 2020 15 UTC at 39°N, 73°W, e)-h): 29 January 2021 15 UTC at 36.8°N, 75.5°W, j)-l): 3 February 2021 14 UTC at 35.5°N, 75.5°W, m)-p): 5 March 2021, 11 UTC at 38.2°N, 74°W (am) and 15 UTC at 38.65°N, 73.5°W (pm), and q)-t): 8 March 2021 trajectory initialized at 15 UTC, 35.2°N, 74.5°W.

Along the flight tracks, SST increases can exceed 10 °C at the western edge of the Gulf Stream (Fig. 3b). The SSTs reach maximum values near 24 °C, decreasing slightly further eastward by a

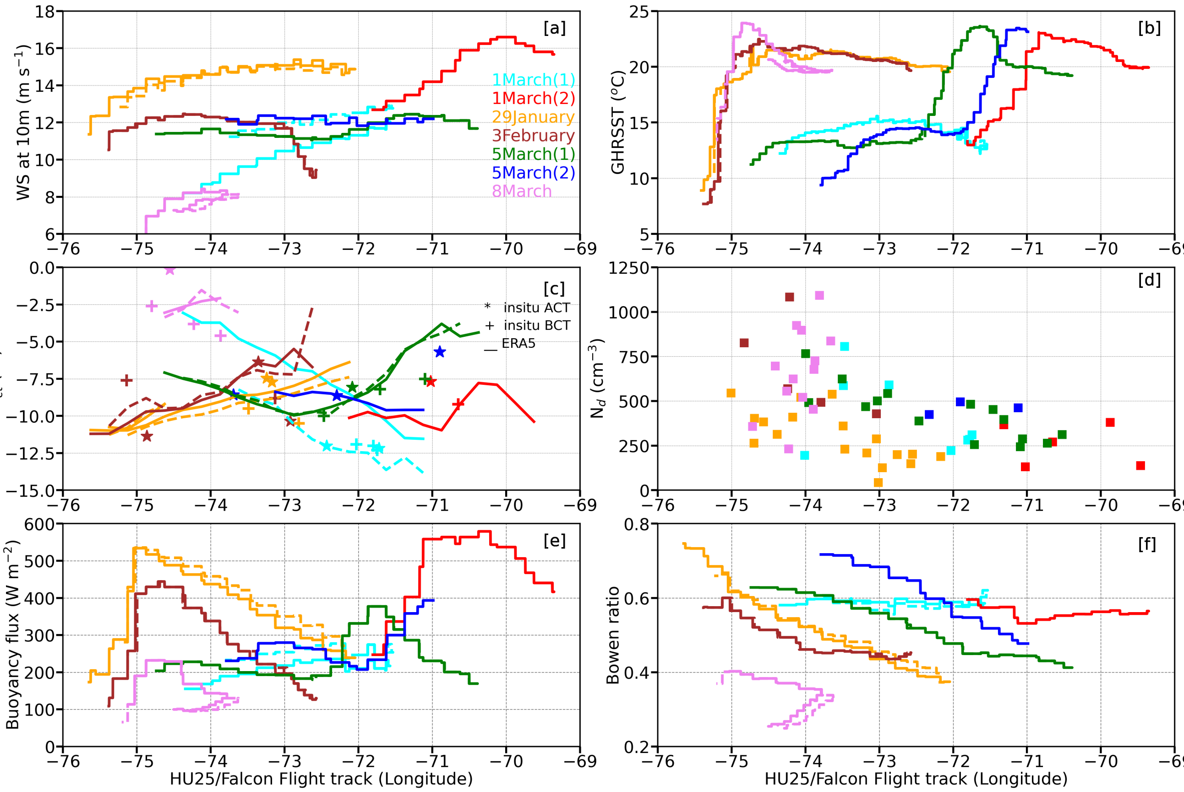

FIG. 3. Meteorology and N_d along the Falcon flight tracks as a function of longitude: a) 10m ERA5 wind speed, b) SST, c) *in situ* and ERA5 T_{ct}, d) Leg-mean N_d (ACB and BCT), e) ERA5 buoyancy fluxes and f) ERA5 Bowen ratio, for outbound and inbound (return) flight tracks (solid and dashed lines, respectively). Morning/afternoon flights on 1 and 5 March indicated by (1) or (2) respectively.

few degrees. Cloud top temperatures (T_{ct}s) increase more slowly but consistently with fetch, from minimum T_{ct}s of ~ -11 °C near the western end, to ~ -5 °C at the eastern end (Fig. 3c). Buoyancy fluxes and the Bowen ratio are a maximum at the western edge of the Gulf Stream, decreasing further east as air-sea temperature differences reduce (not shown). *In-situ* leg-mean N_d decrease with distance offshore from over 1000 cm^{-3} in places to ~ 200 cm^{-3}. The earliest CAO within the year, on January 29, 2021, experienced the strongest surface wind speeds, surface fluxes, and M values of the five days, while the latest CAO, on 8 March, 2021 was the weakest of the five days, inferred from M and the wind speeds. Corresponding values along the Lagrangian trajectories correspond well to those perceived during the flights (Fig. S2). This supports the steady-state assumption that the *in situ* information along the flight track can serve as a proxy for the Lagrangian evolution, despite the differences in air and aircraft speeds. Dropsonde profiles of temperature, θ

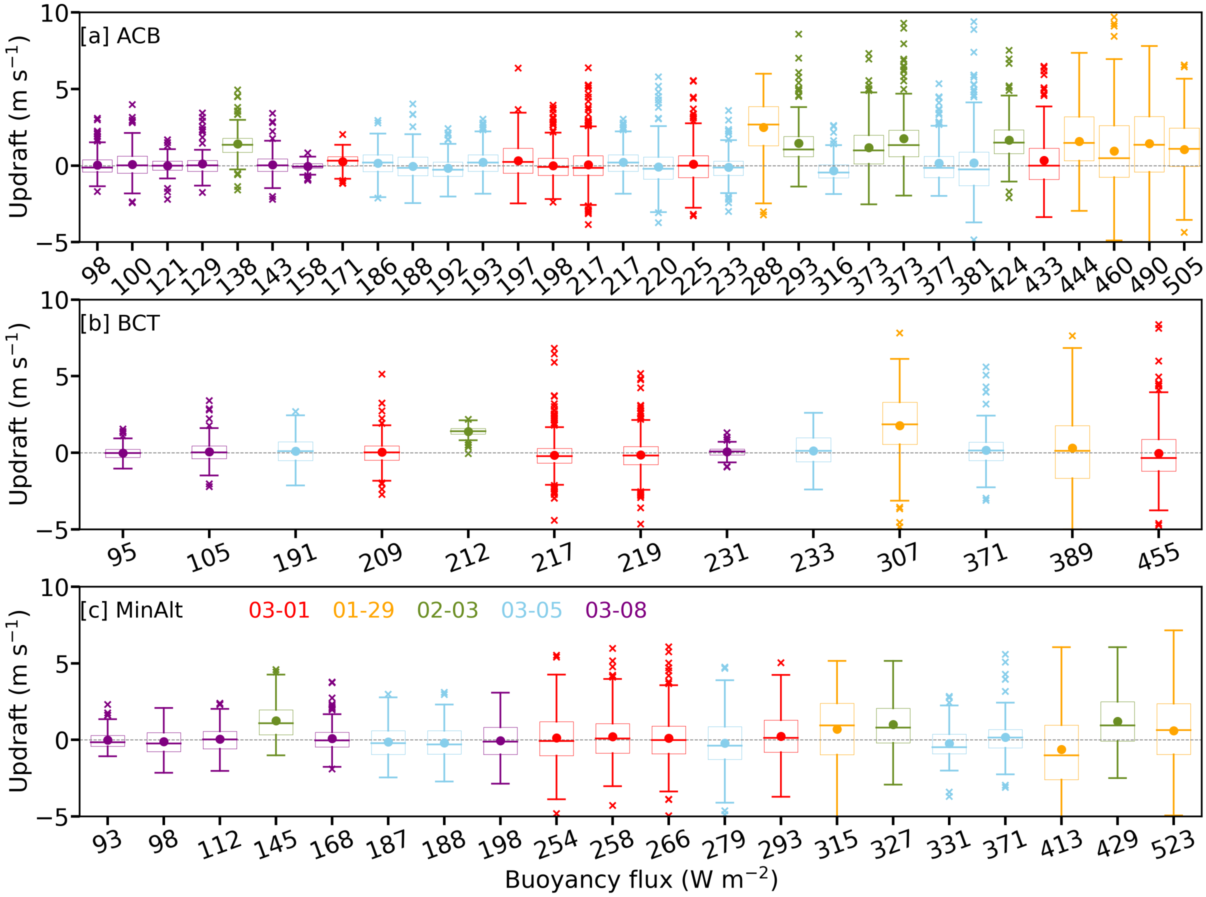

FIG. 4. Histograms of 1 Hz vertical velocities as a function of the buoyancy fluxes for a) above-cloud-base, b) below-cloud-top, and c) minimum altitude level legs. Colors indicate flight date. Means indicated by filled circles, medians and ± 25% percentiles indicated by lines.

and relative humidity for each day indicate boundary layer deepening and near-surface warming as the air masses advect to the east. The relative humidity profiles suggest boundary layers often remain well-mixed (Fig. S3).

Updraft strength increases with the surface buoyancy fluxes, meaning the updrafts are strongest at the eastern edge of the Gulf Stream (Fig. 4). The upper quartile of the updrafts often exceed two m s^{-1} (see also Fig. S4), during the MinAlt, ACB, and BCT level legs, with maximum individual 1Hz values reaching ten m s^{-1}. The afternoon flight on January 29, 2021 sampled the strongest updrafts of the five flight days, followed by 3 February, 2021. One-second downdrafts reach minima of -5 m s $^{-1}$, with the lowest quartile occasionally stronger than -2 m s^{-1} . Updrafts were strongest above-cloud-base (Fig. 4). We will return to Figs. 4 and S4 during the description of the individual days.

4. Microphysical characterization of the five days

The microphysical characteristics of each day are depicted similarly. Initially, a satellite image is superimposed with the flight track using the color-coding conventions of Fig. 1, followed by height-time series of the flight tracks, their *in situ* temperatures, and the location of selected time-stamped 2DS imagery indicated on the flight tracks. Profiles of microphysical quantities are shown for 1 March 2020, 29 January 2021 and 3 February 2021, with profiles from 5 and 8 March 2021 shown in the Supplement.

a. 1 March 2020

1) MORNING

The morning flight paralleled the western edge of the Gulf Stream, sampling perpendicular to the dominant boundary layer flow. The flight nevertheless first sampled clear air, then thin cloud that continued to deepen, into a region with MODIS-derived LWPs of 100-200 g m^{-2}, where a circle of 11 dropsondes was released (Fig. 5). Rimed ice was already noticeable within a thin cloud of primarily small super-cooled droplets (Fig. 5c, left-hand image) at an *in situ* temperature of -8 °C (Fig. 5b) and leg-mean N_d exceeding 800 cm^{-3}. The proximity to upstream clear air suggests primary ice nucleation occurred. A nearby ACB leg during the return leg (16.1 UTC, Fig. 5e) sampled small super-cooled droplets but no ice.

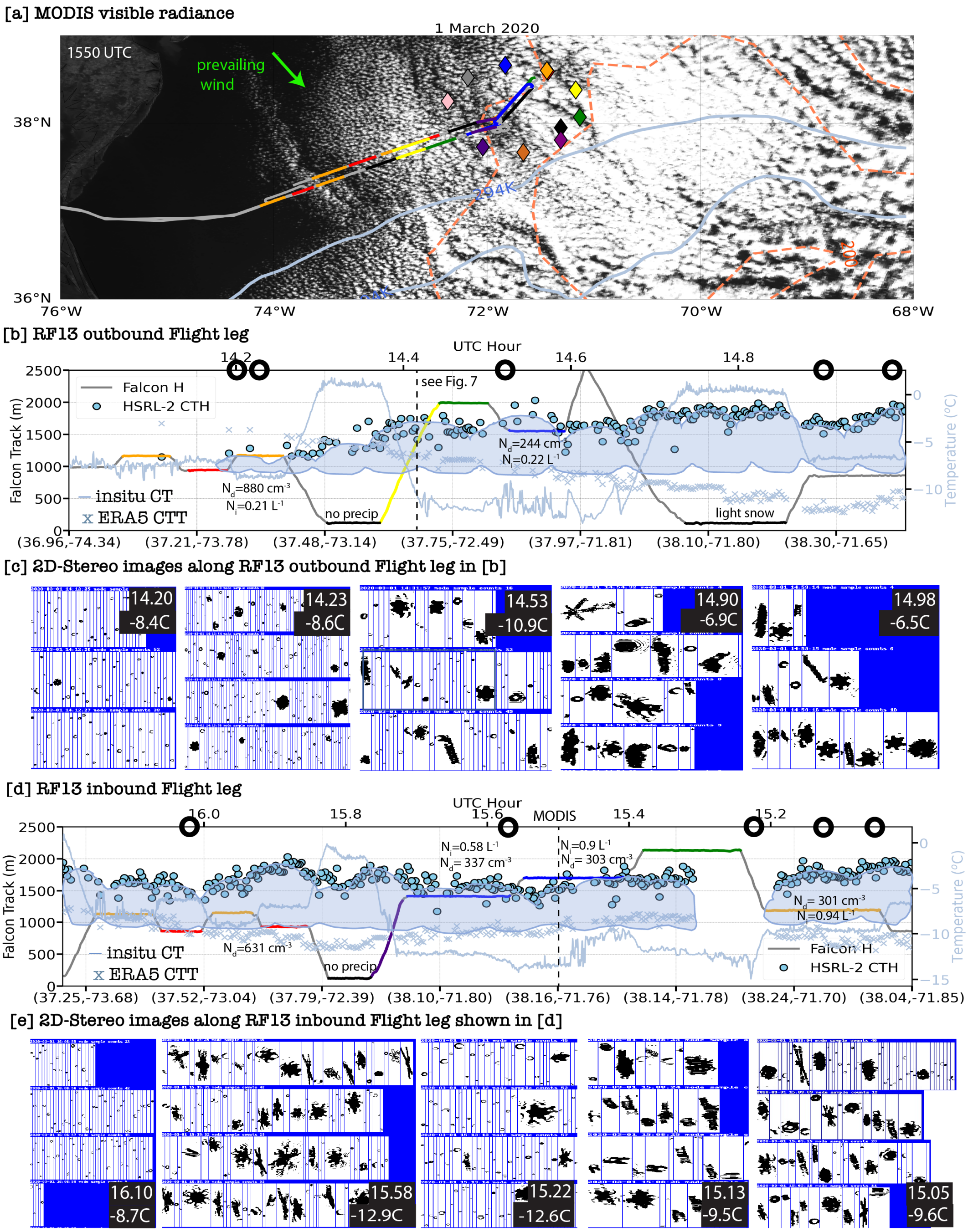

FIG. 5. 1 March 2020 morning flight (RF13). a) MODIS visible imagery with flight track superimposed, color-coded according to Fig. 1 and dropsondes (triangles). SST contour of 294K in blue lines, MODIS LWPs of 100 and 200 g m^{-2} in dashed orange lines. b) HSRL2-inferred cloud top height (circles), altitude flight path (color-coded), *in situ* temperatures and ERA5 T_{ct} (light blue line and crosses; right-hand y-axis) for the outbound flight. Circles along upper x-axis correspond to 2DS imagery times in c). d)-e): same as b)-c) for the return inbound leg; time along upper x-axis increases from right to left. b), d): N_d, N_i indicated for ACB (orange) and BCT (blue) legs. Cloud depiction is a schematic.

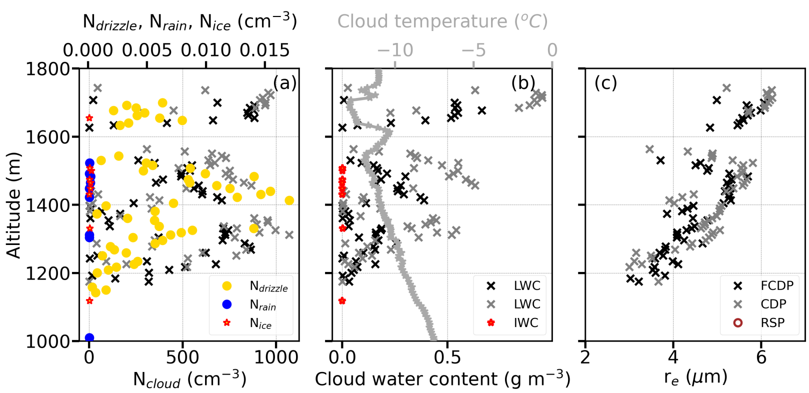

FIG. 6. *In-situ* ascent of 1 March 2020 morning (RF13) at 14.4 UTC, 37.65°N, 72.72° E of a) cloud, drizzle, rain and ice number concentrations (black asterisks, yellow, blue and red filled circles respectively, FCDP+2DS combined distribution), b) cloud water contents (CDP and FCDP, grey and black asterisks, LWP= 84 and 161 g m^{-2} respectively) and temperature (grey), and c) mean FCDP and CDP droplet effective radius (r_e, black and grey asterisks respectively).

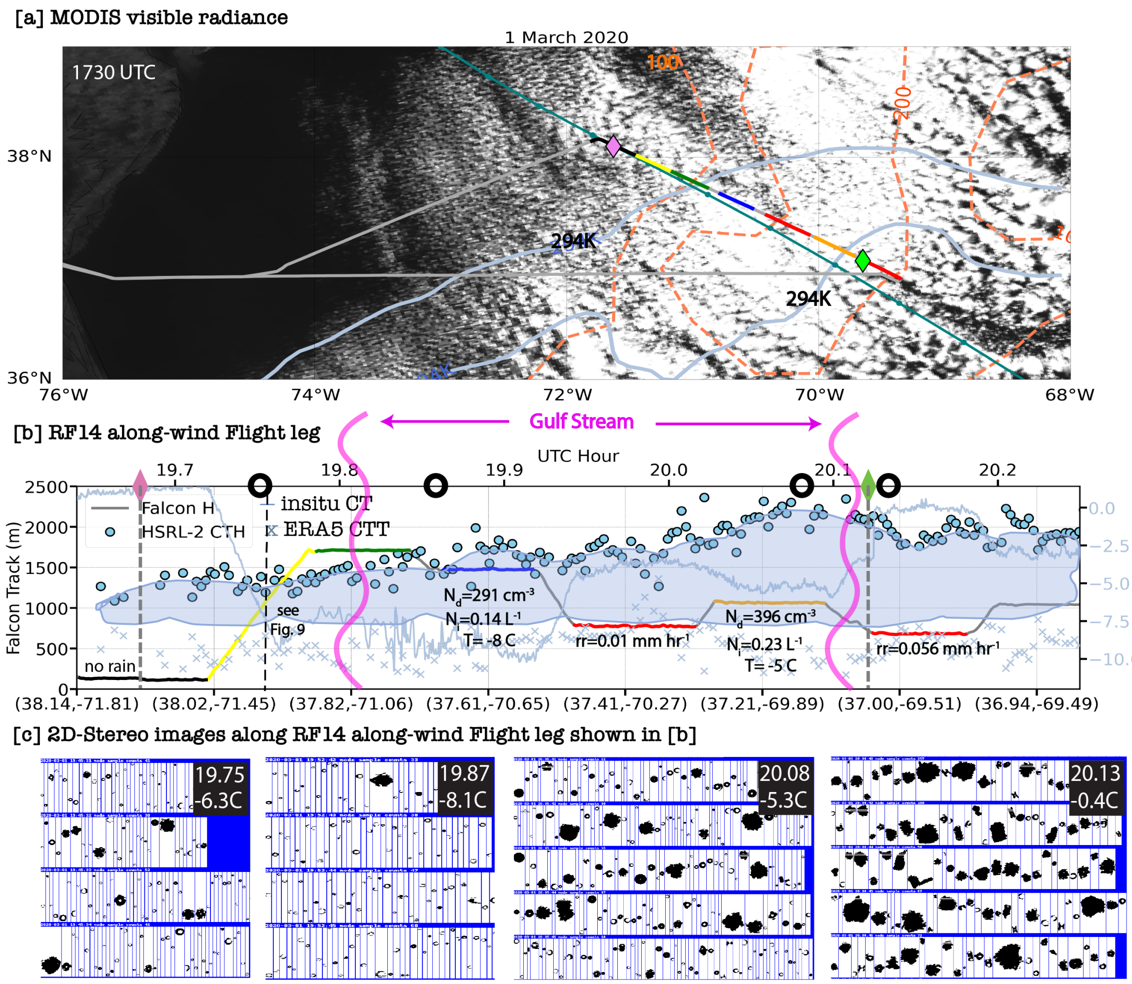

FIG. 7. 1 March 2020 afternoon flight (RF14). Similar notation to Fig. 5. No RSP data. 19.75 UTC ascent profiled in Fig. 8. Two dropsonde locations and times indicated with diamonds. Curved pink lines indicate location of the Gulf Stream (294K SST contour) throughout.

Further within the more developed, stratiform cloud region, snowflakes and large rimed ice particles occur under an ERA5-derived T_{ct} of ~ -12 °C. T_{ct} is near -13 °C for much of the cloud sampling (see *in situ* temperature trace at 14.6 UTC), and dendritic ice growth appropriate to this temperature range is clearly evident throughout the flight. Cloud top heights reach ~ 1.8 km. N_i reaches almost 1 L^{-1} at the northeast end of the flight, too large to still be primary ice production. Only slight precipitation (snow and a few rimed ice particles) is detected on the easternmost MinAlt leg at 14.8 UTC, at temperatures barely above 0 °C. The leg-mean N_d decreased within the more developed cloud near the dropsonde circle, consistent with dilution through cloud top entrainment (Tornow et al. 2021). Dropsondes show mostly well-mixed boundary layers (Fig. S3). The flight did not reach beyond the overcast stratiform cloud region, nor entered above the demarcated Gulf Stream.

The first profile, an ascent through cloud with a LWP of ~ 100 g m^{-2} (Fig. 6), shows an inversion-capped cloud layer reaching ~ 1.5 km, with a separate thin cloud layer between 1.6 to 1.8 km. Surface buoyancy fluxes reach 200 W m^{-2} (Fig. 3e), supporting vertical velocities of 2-4 m s^{-1} (Figs. 4 and S4). Although such updrafts may be strong enough to puncture an existing cloudtop inversion and form a new cloud layer aloft, none of the dropsondes show such a marked temperature structure (Fig. S3). Instead, the dropsondes captured a range of inversion heights, often capped by multiple stable layers. This is more consistent with a range of cloud top heights and likely the plane exited one convective cell and entered the top of another. No ice was detected in the uppermost, coldest cloud layer. Cloud-top r_e remain below six μm, consistent with N_d exceeding 700 cm^{-3}. Some ice was sampled within the profile near the top of the middle layer, at temperatures between -10 to -12 °C, with vapor-driven particle growth evident nearby in 2DS imagery in the same temperature range (e.g., snowflakes at Fig. 5c at 14.53 UTC and the next hour). N_i and IWCs are highest at cloud temperatures between -9.5 °C and -12.5 °C, outside the HM temperature range for SIP, but colocated with some drizzle and the liquid water content (LWC) maximum (Fig. 6), suggesting another rime-related SIP may be active.

2) Afternoon

Conditions during the afternoon flight were visually similar to the morning flight, but now the research flight was well-aligned with the boundary layer flow, crossing over the 294 K SST

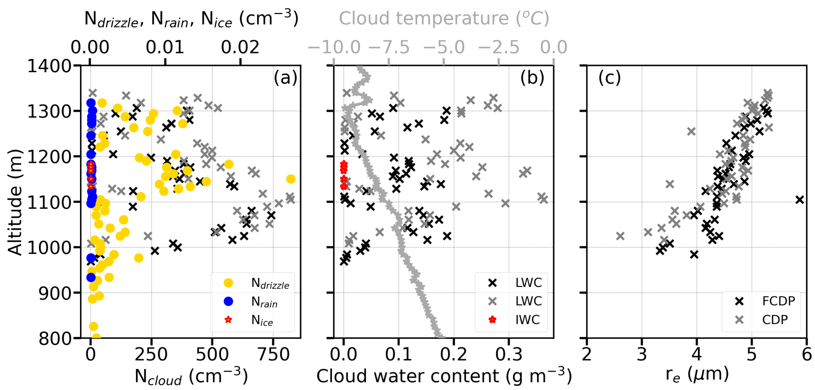

FIG. 8. 1 March 2020 afternoon (RF14) *in-situ* ascent at 37.95°N, 71.31°E, 19.75 UTC of a) cloud, drizzle, rain and ice number concentrations, FCDP+2DS, (b) cloud water content and temperature (CDP and FCDP, grey and black asterisks, LWP= 30 and 51 g m^{-2} respectively), and (c) droplet effective radius (r_e).

contour outlining the Gulf Stream at 19.8 UTC and briefly experiencing the cloud transition into more open-celled convection past the eastern edge of the Gulf Stream at 20.2 UTC (Fig. 7). Just before the Gulf Stream, an ascending profile sampled rimed ice within a layer of predominantly super-cooled water droplets at temperatures ~ -6 °C (Fig. 7c, first image). N_d decreases with altitude and is slightly less than in the morning (Fig. 8; 250-400 cm^{-3} versus 500-800 cm^{-3}). The temperature inversion is capped by at least one additional stable layer similar to the dropsonde profiles, consistent with the idea that the boundary layer deepening may be occurring in discrete intervals as opposed to a smooth increase in height.

Just east of the Gulf Stream, MODIS LWPs reach 200 g m^{-2}, with cloud top heights reaching 2.3 km (Fig. S3, lime-green dropsonde) above a slightly stable boundary layer ($\frac{\partial\theta}{\partial z}$ ~ 2 K km^{-1}). The cloud base warms as the flight progresses, with the first below-cloud-base leg (BCB, red) occurring at ~ -3 °C and the second near 0 °C, despite similar altitudes of ~ 700 m. Light rain is mixed with some aggregates during the first BCB leg (not shown). Rain increases to 0.056 mm hr^{-1} in the second BCB leg amidst large snow aggregates falling towards even warmer temperatures (Fig. 7c, last image). Thus rain is measured just prior to the transition region to a more open-celled cloud structure. Rimed ice particles co-exist with supercooled droplets in the HM temperature range (2DS image at 20.08 UTC in Fig. 7c and Fig. 8), with some (poorly-resolved) columns apparent at 20.13 UTC. N_i increases towards the east as the clouds deepen, as does the rainrate below cloud base (Fig. 7b).

b. 29 January 2021

This CAO is the earliest within the seasonal cycle, with the 294 K SST contour barely reaching the ACTIVATE domain from the south (Fig. 2e). The morning and afternoon flights follow similar boundary layer flows, sampling mostly visually-overcast regions with MODIS LWPs > 250 g m^{-2} and just able to reach the open-celled cloud structure east of the Gulf Stream. ERA5 10-m winds exceed 14 m s^{-1} in places (Fig. 3a), supporting buoyancy fluxes > 500 W m^{-2} at the western GS edge (Fig. 2h), and 1 Hz ws exceeding 5 m s^{-1} (Figs. 4, S4). The morning-only high-flying King Air plane released two dropsondes, near the eastern and western edges of the Gulf Stream respectively, separated by a distance of $\sim$ 100 km. These indicate a deepening of a relatively well-mixed boundary layer from $\sim$ 1.7km to $\sim$ 2 km (Fig. S3), with the near-surface relative humidity decreasing to 50% - dry enough to desicate sea salt (Ferrare et al. 2023).

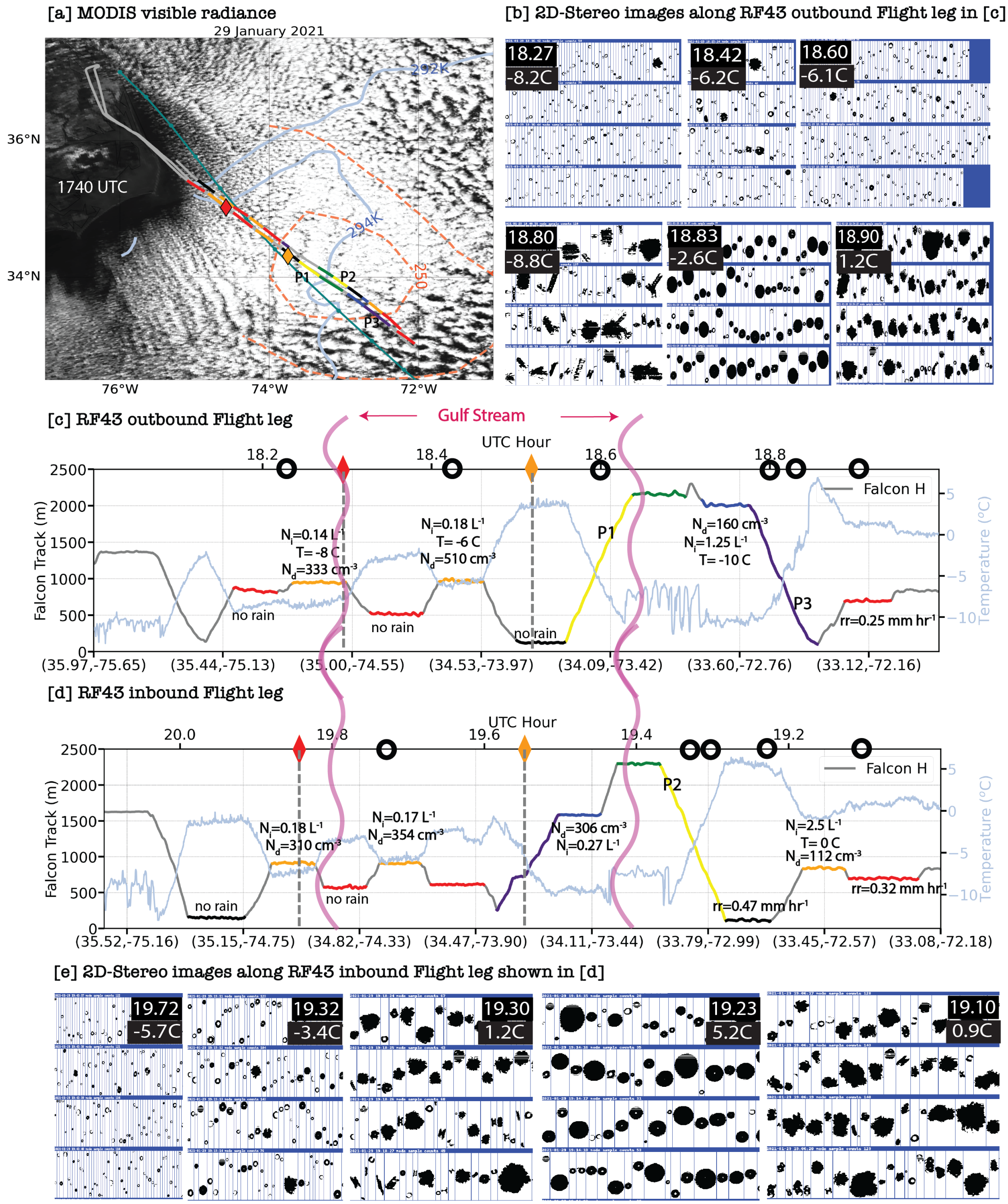

356 FIG. 9. 29 January 2021 afternoon (RF43). Similar notation to Fig. 5. Morning dropsonde locations shown.
357 See Fig. 10 for *in situ* profiles P1, P2 and P3.

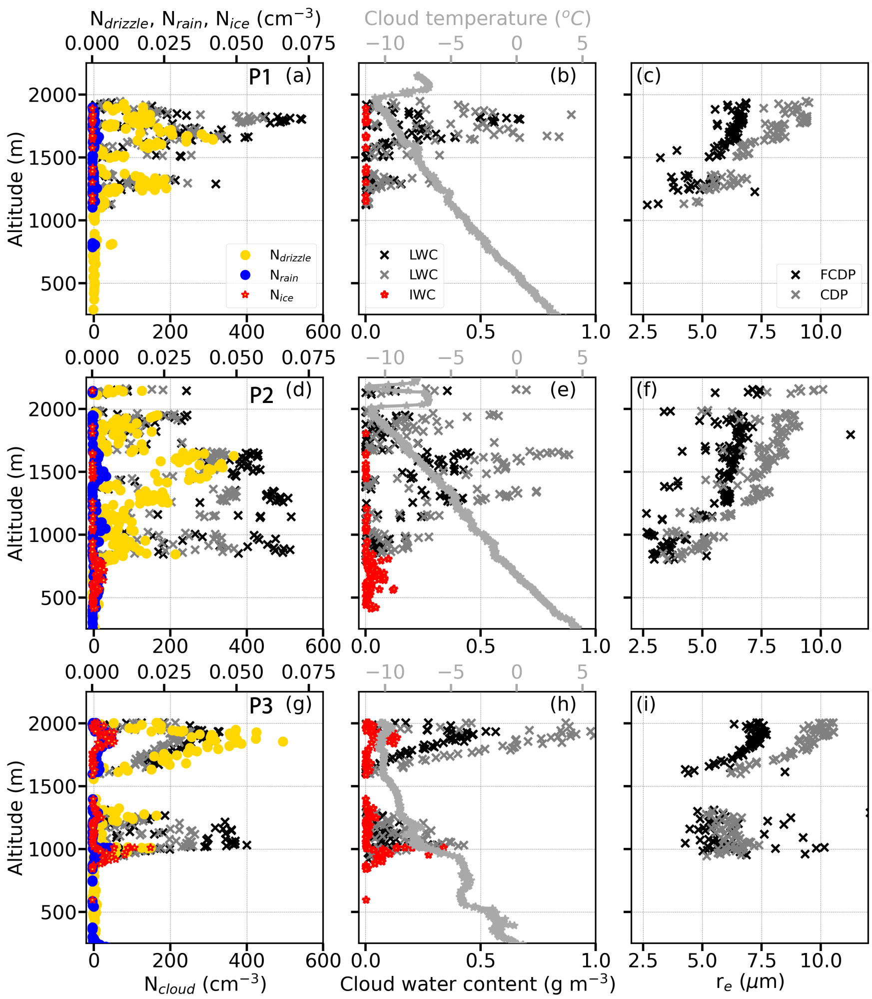

FIG. 10. 29 January 2021 afternoon (RF43) *in-situ* profiles organized from west (top) to east (bottom). a)-c): P1, ascent at 18.6 UTC, 34.13°N, 73.46°W (FCDP+2DS, CDP+2DS LWP=93, 225 g m^{-2} resp.) over the eastern flank of the Gulf Stream. d)-f): P2, 19.35 UTC ascent at 33.83°N, 73.04°W (FCDP+2DS, CDP+2DS LWP=121,260 g m^{-2} resp.), just east of the eastern GS 294 K SST contour. g)-i): P3, descent at 18.8 UTC, 33.43°N, 72.55°W (FCDP+2DS, CDP+2DS LWP=154, 305 g m^{-2} resp.), further east of the Gulf Stream. Conventions as in Fig. 6.

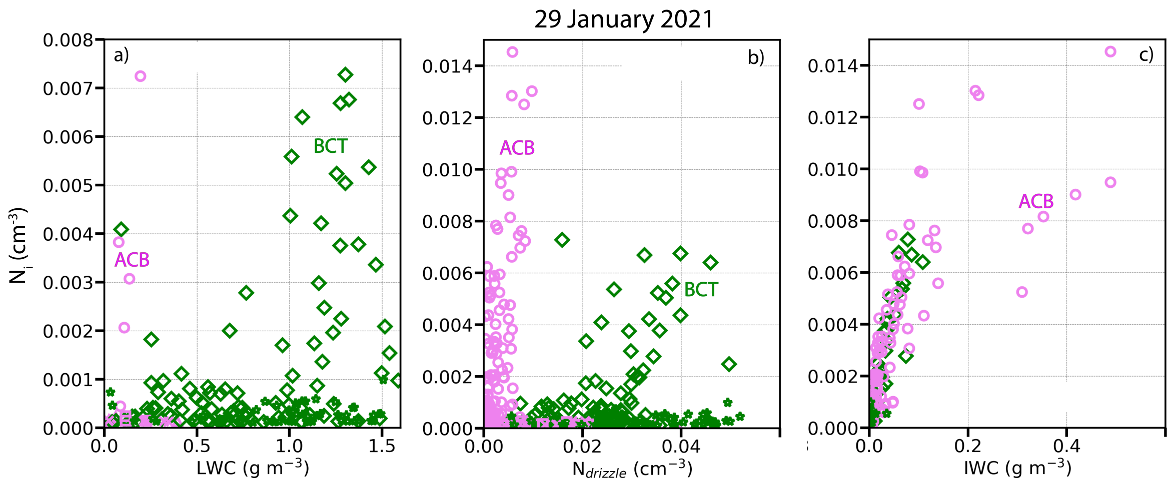

FIG. 11. N_i vs a) LWC, b) $N_{drizzle}$, and c) IWC for the ACB (pink) and BCB (green) legs from 29 January 2021 (RF43), using 1Hz data. Note y-axis range for N_i differs between a) and b),c).

The locations of the morning dropsondes are superimposed on the *in situ* information collected during the afternoon RF43 flight in Fig. 9. Prior to crossing over the western GS edge at $\sim$ 18.3 UTC, the first within-cloud ACB leg measured a leg-mean N_d of 330 cm^{-3} at a temperature of -8.2 °C. A rimed/aggregated ice particle is already present within the cloud of small droplets (see first image in Fig. 9b). The proximity to clear-sky upwind again points to primary ice production, as opposed to secondary. Deeper clouds further east reach an *in-situ* T_{ct} near -10 °C at 18.75 UTC. Rimed and aggregated snow particles are detected, along with a few columns (see e.g. 2DS image at 18.8 UTC). The thickest cloud is situated at and east of the eastern GS edge. By then, the BCB leg temperature has risen to 2 °C, and leg-mean rain rates reach 0.25 mm hr^{-1}, increasing to 0.47 mm hr^{-1} for the lower MinAlt leg (note these rainrates are based on 1Hz samples exceeding 0.01 mm hr^{-1} only). Snow aggregates below cloud base become rain by 150 m above the ocean surface, preceeding the transition to a more open-celled cloud morphology.

Three *in situ* profiles occur within 45 minutes and 110 km of each other, either directly over or slightly east of the Gulf Stream (Fig. 10). These are shown arranged from east to west (top to bottom) in Fig. 10, with profile P3 preceeding profile P2 in time. For all three profiles, the T_{ct} and cloud top height remain at -10 to -11 °C and 2 km respectively. Precipitation in both the ice and liquid phase increase with fetch. *In situ* profile LWPs increase from 230 to 440 g m^{-2}, yet *in situ* cloud-top effective radii remain at 9 μm or below, because of the high number of droplets (maximum N_d ranges between 400-500 cm^{-3}). The profiles appear to sample two (or more) distinct cloud layers, although this may reflect slant-path ascent wherein up- and downdrafts produce different cloud bases.

Profile P1, an ascent at 18.6 UTC over the eastern GS, samples a well-mixed boundary layer in stratiform conditions (Fig. 10a-c). The 0 °C level is at ~ 500 m, below the lower cloud base at 1.2 km, and the cloud top is strongly capped by a 5K temperature inversion (Fig. 10b). N_d increases to 550 cm^{-3} near the upper cloud top, within the highest LWCs of the profile. The increase in N_d with height suggests the N_d is reduced lower down primarily through collision-coalescence. Despite cloud-top r_e of only ~ 8 μm, some drizzle is present higher up, capable of initiating collision-coalescence, and some ice particles are detected at temperatures between -4 to -10 °C.

The ascent profile P2 approximately 50 km further east occurred at 19.35 UTC during the return flight. A lower cloud base at approximately 800 m compared to P1 suggests the plane went through an updraft bringing up moist air (Fig. 10d-f). An additional thin cloud layer exists at 2.2 km altitude above the existing inversion, similar to Fig. 6. Buoyancy fluxes exceeding 500 W m^{-2} (Fig. 2h) coincide with updrafts in the preceeding ACB leg that reached 5 m s^{-1} in places, for a leg-mean w of 3.5 m s^{-1}. These may have punctured through the capping cloud inversion to produce the thin cloud layer aloft. N_d decreases from 600-650 cm^{-3} at cloud base to ~ 300 cm^{-3} near cloud top, also consistent with dilution through entrainment (Tornow et al. 2022).

Graupel coexists with super-cooled water at the upper levels. The 0 °C level has risen 100-150 m from the location of P1, to 600-650 m, with a stable layer below the cloud base indicating melting-induced cooling. Larger snow aggregates are apparent at temperatures slightly above melting, transitioning to rain by the 5 °C of the MinAlt leg (Fig. 9e, middle three images). The MinAlt leg-mean rainrate is relatively high at almost 0.5 mm hr^{-1}. Both the IWC and N_i increase near or just below the cloud base within the P2 profile. Prior to P2, on an ACB leg, the highest N_i of the five flight days, 2.5 L^{-1}, was measured at near melting temperatures (Fig. 9d, 19.15 UTC). 2DS imagery at 19.1 UTC indicates many ice (graupel) particles and snow aggregates of different sizes. We speculate surface melting on ice particles is enhancing ice aggregation, thereafter breaking up into more N_i through collisions (Fabry and Zawadzki 1995).

Further east by 50 km, the descent profile P3 at 18.8 UTC on the outgoing flight took place just west of an open-celled cloud structure (Fig. 10g-i). The descent followed a BCT leg with a leg-mean N_i of 1.25 L^{-1} (1 Hz $N_i > 0$ samples only) at a temperature of -10.5°C. During the descent, 2DS imagery first indicates large graupel and aggregates (18.8 UTC in Fig. 9b) followed by rain drops by 18.83 UTC. The subsequent BCB leg samples mostly aggregates and graupel at 18.9 UTC (Fig. 9b) but with a leg-mean rainrate of 0.25 mm hr^{-1}, at 1 °C. The *in situ* P3 temperature profile is erratic (Fig. 10h), suggesting icing may have at times influenced the aircraft temperature sensor.

Fig. 10g-h show a clear correlation between N_i and $N_{drizzle}$ at the upper levels, as well as between IWC and LWC, suggesting rime-splintering is still occurring at temperatures too cold for HM ice production. Droplet shattering would be inefficient given the mean effective radius of ~8 μm. Riming, besides increasing the IWC, also increases variations in the particle fall speeds and encourages breakup through graupel-graupel collisions (e.g., 2DS imagery of a spheroid and elongated ice particle together at 18.8 UTC in Fig. 9b). Increased N_i and IWC are also present at cloud base, similar to P2, consistent with enhanced aggregation enabled by a liquid layer on the surface of ice.

Overall the *in situ* data indicate N_i increases with fetch to the east, shifting to the liquid phase near the surface, before thick clouds transition into more open-celled structures. The highest N_i documented within the five days occurred on this day. N_i is clearly enhanced at both upper and lower clouds levels (see Fig. 10g in particular), summarized in Fig. 11, and more than one SIP mechanism appears to be at play. At upper levels, N_i increases with increasing LWC, $N_{drizzle}$ and IWC at temperatures ~ -10 °C (Fig. 11), consistent with riming followed by collisional breakup, and maybe droplet freezing, although the small drop sizes discourage the latter. Near or slightly below cloud base, at temperatures near 0 °C, the most pronounced increase in N_i occurs with IWC (Fig. 11c), a relationship that seems best explained by a surface layer of quasi-liquid enhancing aggregation and thereby N_i through collisional breakup. Precipitation doesn't set in until the eastern GS edge, perhaps delayed by the high N_d. By then, the air near the surface is warm enough that snow aggregates melt into rain before reaching the surface (e.g., 19.10 UTC BCB leg and 19.23 UTC MinAlt leg 2DS imagery in Fig. 9e).

c. 3 February 2021

Both planes participated in this morning-only flight, flying through/over thick stratiform cloud above the Gulf Stream for which MODIS-derived LWPs exceed 200 g m^{-2} in places (Fig. 12), reaching the cloud transition region. The FCDP failed from 15.1 UTC to 16.1 UTC, increasing reliance on the CDP data. The stratiform cloud is visually the brightest of the five flight days (Fig. 2), with leg-mean N_ds exceeding 700 cm^{-3} at the western GS edge. The Gulf Stream was broader than on Jan. 29, and surface winds of 12 m s^{-1} were weaker than those on January 29, 2021, by 2-3 m s^{-1} (Fig. 2). Buoyancy fluxes exceeded 400 W m^{-2} at the western GS edge, corresponding to a 14 K air-sea temperature difference. These continue to support vertical velocities exceeding 5 m s^{-1} (Figs. 4 and S4).

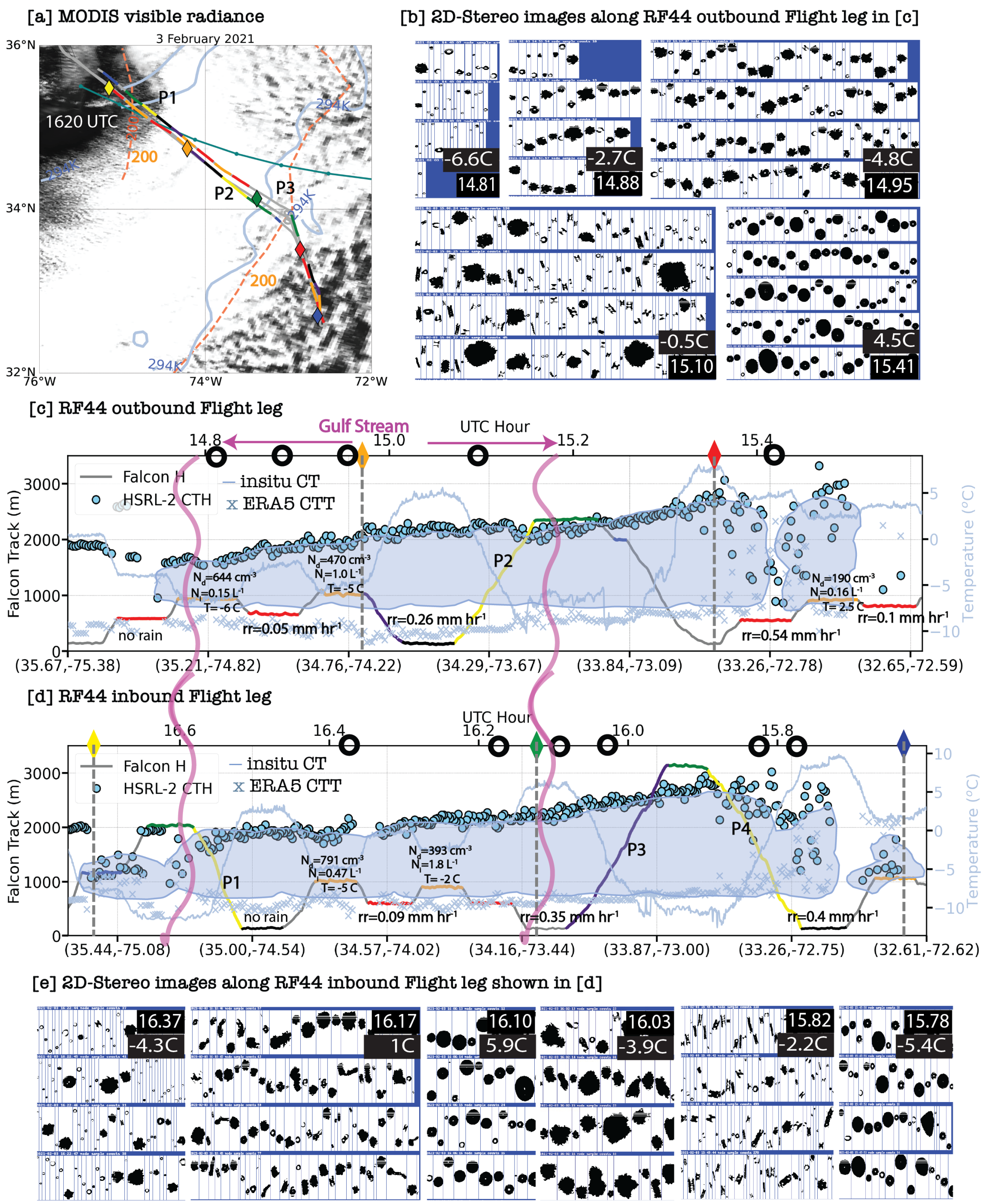

FIG. 12. 3 February 2021 morning (RF44). Similar notation to Fig. 5. FCDP cloud probe iced from 15.1 UTC until midway through P3 descent at 16.1 UTC (profiles shown in Fig. 14).

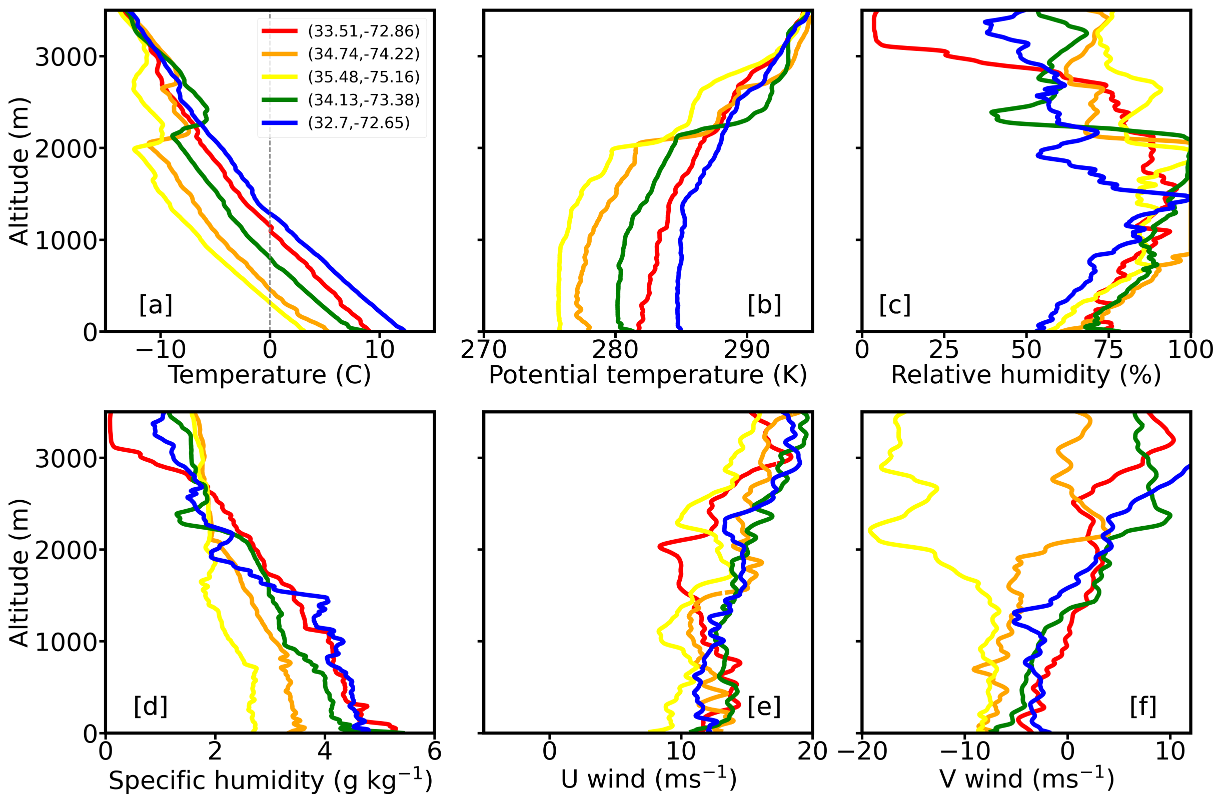

FIG. 13. 3 February 2021 morning (RF44) dropsonde profiles of a) temperature, b) potential temperature, c) relative humidity, d) specific humidity, e) zonal wind, and f) meridional winds. Colors follow the diamonds in Fig. 12: yellow dropsonde is west of the GS, orange over the middle of the GS, green at GS eastern edge, red and blue just before and within the open-celled cloud structure, respectively.

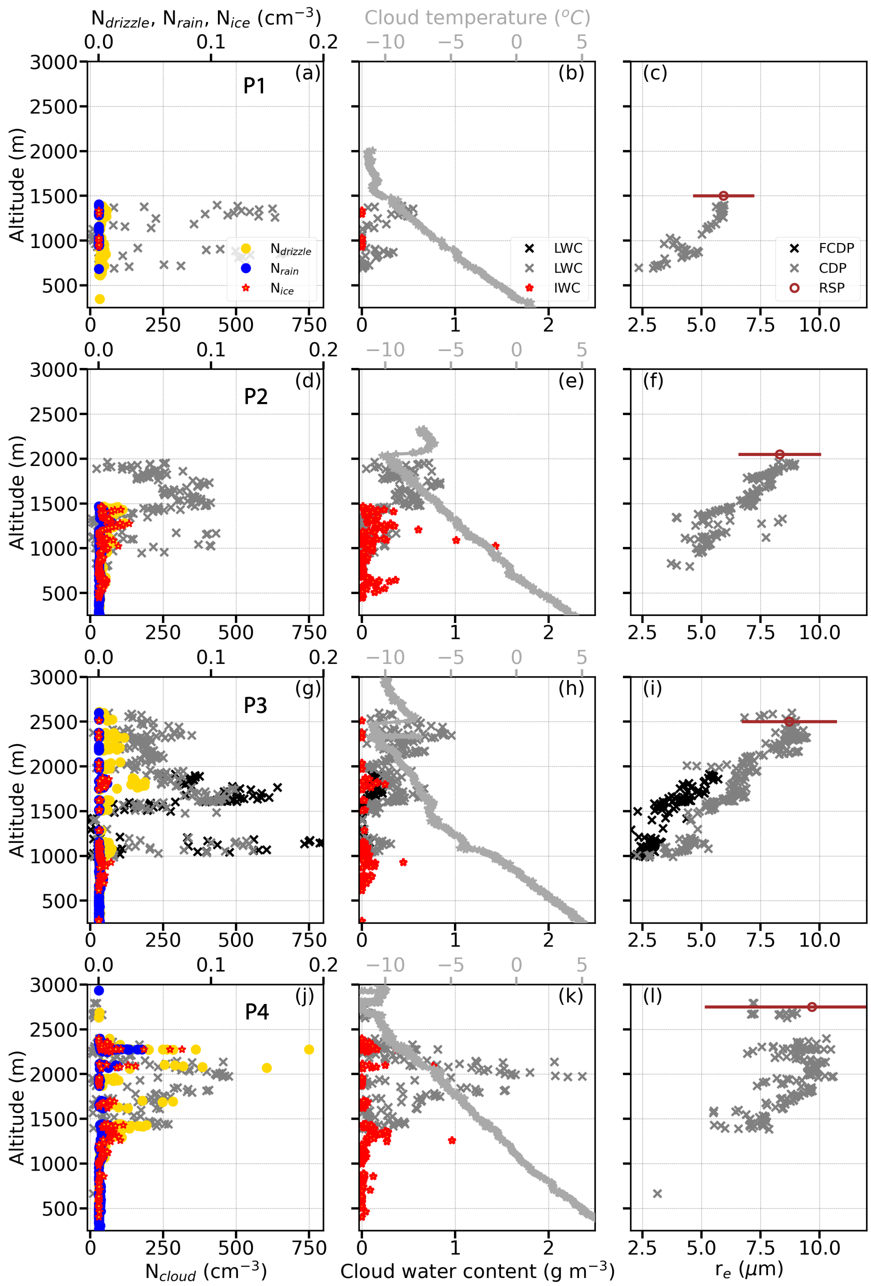

FIG. 14. Four *in situ* profiles from 3 February 2021 morning flight (RF44), organized from west (top) to east (bottom). FCDP (black asterisks in g)-i)) was iced but for a portion of the P3 descent. a)-c): P1 ascent at 16.55 UTC at 35.11°N, 74.67°W on the return (inbound) leg (CDP+2DS LWP=297 g m^{-2}). d)-f): P2 ascent at 15.1 UTC, 34.27°N, 73.65°W during outbound leg (LWP=526 g m^{-2}). g)-i): P3 descent at 15.95 UTC, 33.91°N, 73.07°W, on return (inbound) leg (LWP=400 g m^{-2}). j)-l): P4 ascent at 15.8 UTC, 33.36°N, 72.80°W, on return leg (LWP=95 g m^{-2}). Same labeling conventions as in Fig. 6. LWPs based on corrected CDP data.

Cloud top temperatures are consistently near -10 °C throughout the flight (Fig. 12), despite cloud top heights simultaneously rising to over 2.5 km, the highest of the five flight days. This indicates a warming boundary layer with fetch. Five dropsondes, straddling the GS within 350 km of each other, detail the evolution of the boundary layer (Fig. 13). Furthest west, a well-mixed clear-air boundary layer of one km depth and a potential temperature (θ) of 276 K overlaid an SST of ~ 286 K (Fig. 2). The spatially-subsequent sounding (orange line), ~ 120 km further east over the Gulf Stream, also sampled a mostly well-mixed lower boundary layer now warmed to a θ of ~ 278 K. The SSTs have increased more, however, reaching 290 K, so that the air-sea temperature difference has increased to 12 K. The inversion height has increased only slightly, to ~ 2 km. East of the dropsonde, rimed ice was already sampled during the first ACB leg, in thin cloud at a temperature of -6.6 °C (Fig. 12b, 14.81 UTC) for which the leg-mean N_d exceeded 600 cm^{-3}. An interesting feature is a further increase in θ by ~ 1 K within the lowest 200 m, despite the presence of snow (2DS image at 15.10 UTC in Fig. 12b). The precipitation habit in the nearby MinAlt leg (Fig. 12c) is melting snow and liquid, at 3 °C, for a leg-mean rainrate of 0.26 mm hr^{-1}. The near-surface θ increases suggests the thermal fluxes off of the ocean are strong enough to override any evaporation-induced cooling. Winds above the capping inversion shift to almost southerly, increasing the ability for shear to induce entrainment.

The dropsonde at the eastern GS edge (green line), is associated with near-surface rainrates of ~ 0.35 mm hr $^{-1}$ (Fig. 12b), yet the lower boundary layer has warmed further to a θ of 280 K in the lowest one km, with the capping inversion slightly raised to 2.1 km. This profile too shows a distinct warming in the lowest 100 m near the surface, if less pronounced. The subsequent profile (red line), taken on the outbound flight just before the transition to open-celled convection, sampled a more stabilized cloudy boundary layer that had deepened to approximately 2.5 km and incorporated a lower-tropospheric moist layer. The sub-cloud θ has warmed to 282 K. Within the lowest 400 m, a cooling indicative of rain evaporation is now present. This dropsonde is close to open-celled cloud structures further east. The furthest east dropsonde, east of the GS, fell within the open-celled convection, within a well-mixed boundary layer with a θ of 285 K reaching 1.5 km, and twice the specific humidity of the initial sounding. The air-sea temperature differences are still significant at 9 K, but combined with slightly diminished near-surface wind speeds of 10-12 m s^{-1}, the buoyancy fluxes have reduced to < 200 W m^{-2} (Fig. 2).

The dropsondes reveal that the 0 °C level increases from approximately 0.5 km to 1.2 km over a distance of ~ 350 km (Fig. 13a). At the same time, the cloud base height descends throughout the eastward evolution (see ACB legs in Fig. 12). The cloud base temperatures increase from ~ -4 °C at the western GS edge to ~ 3 °C at the eastern GS edge (Table S1). Near-surface precipitation quickly transitions to liquid, and is certainly liquid by the time the cloud deck transitions to an open-celled morphology, with ice columns and snow aggregates still present in the overlying cloud (Fig. 12d, 2DS imagery at 15.82 UTC and 16.03 UTC, as well as at 14.95 and 15.10 UTC). This has implications for surface cold pools, as the fall speeds of rain exceed those for snow, so that more evaporation is likely to occur closer to the surface. Precipitation increases to the east, reaching above 0.5 mm hr^{-1} near the surface at 15.4 UTC, just prior to the transition to a more open-celled cloud morphology, and a surface cold pool is present in the nearby sounding (red dropsonde in Fig. 13b).

The four *in situ* profiles also show the boundary layer deepening, coupled with a rising 0 °C level (Fig. 14). Snow/ice particles remain to temperatures of ~ 3 °C. N_i are higher in the thicker cloud, with ice columns, graupel and supercooled liquid drops present within the HM temperature regime (or warmer, possibly advected in from above). In contrast to the CAO from four days previous, the HM mechanism may be effective in producing ice on this day. The highest N_i occurs where drizzle is most plentiful in furthermost east profile at 15.1 UTC (Fig. 14, bottom row). Droplet shattering likely remains an ineffective SIP mechanism, as the *in situ* r_e near cloud top are 10 μm or lower, matched well by the RSP-retrieved r_e (Fig. A4c). N_i increase with IWC in the ACB level legs (not shown) suggesting collisional breakup can also contribute to the N_i. The RSP retrievals indicate a small but consistent increase in cloud-top r_e with distance offshore (Fig. A4c), while the RSP-derived LWP of 400 g m^{-2} on the outbound leg increases over the thickest stratiform segment to LWPs over 600 g m^{-2}.

d. 5 March 2021

By 5 March 2021, warmer Gulf Stream waters extended further to the northeast (Fig. 2), and a narrowly-defined GS with buoyancy fluxes reaching 400 W m^{-2} was fully transected by both planes during the morning (RF49; Fig. 15), with the afternoon RF50 only reaching the middle of the GS (Fig. 16). Near-surface wind speeds reach 12 m s^{-1}, MODIS LWPs reach 100 g m^{-2}, and maximum leg-mean N_d are near 500 cm^{-3}. These values are all lower than the maxima from 3 February 2021. The dropsonde profiles (7 total, Fig. S3) show a well-mixed boundary layer at the furthest west (19.82 UTC) initially capped at ~ 1.4 km, deepening to ~ 2.2 km by the eastern end. Cloud tops rise by ~ 200 m per degree, with T_{ct} cooling slightly from ~ -8 °C to a minimum of -10 °C.

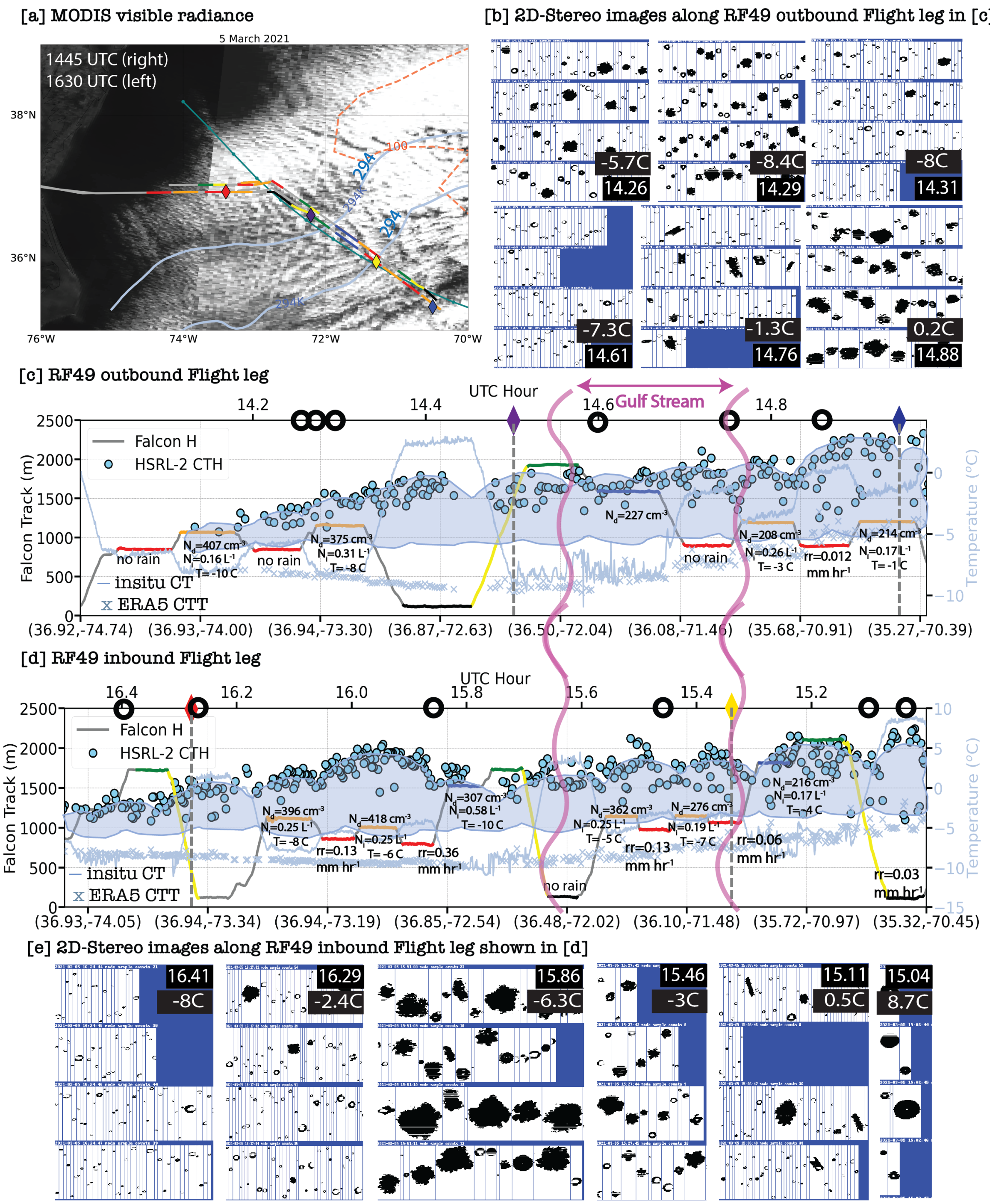

FIG. 15. 5 March 2021 morning (RF49). Similar notation to Fig. 5. First and third ascent partial profiles upon return shown in Fig. S6.

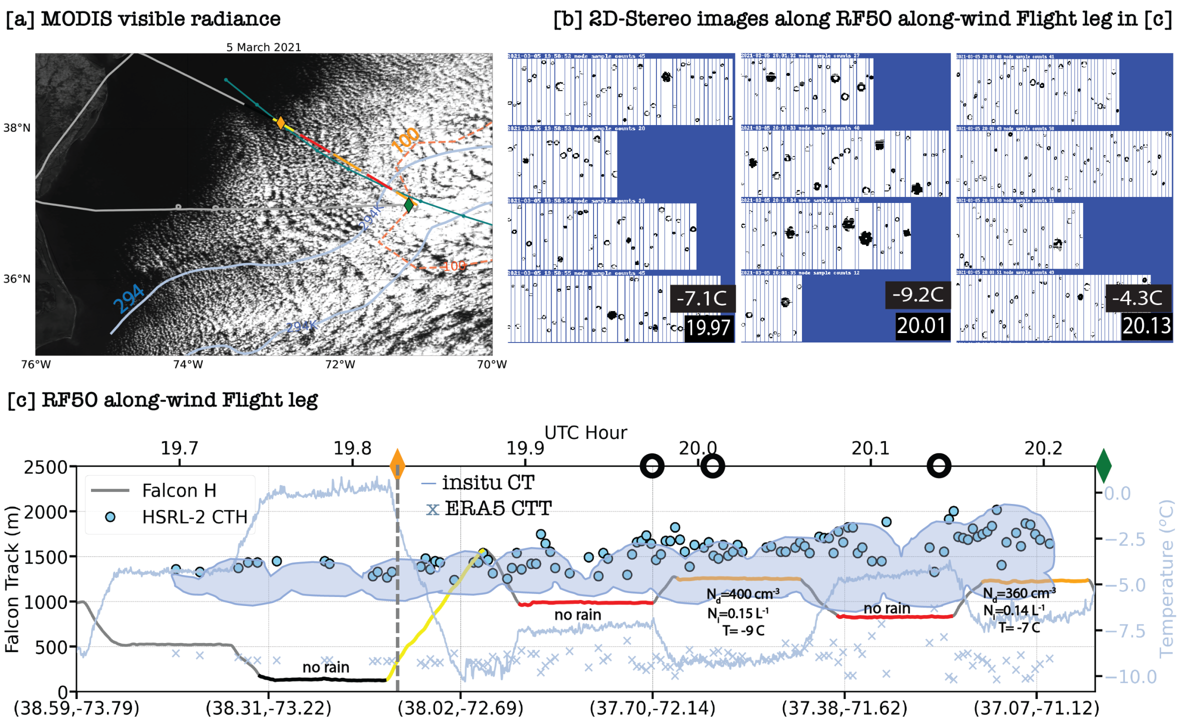

Fig. 16. 5 March 2021 afternoon (RF50). Same conventions as in Fig. 5.

The furthermost east dropsonde crosses 0 °C at 1.1 km, with a cloud base temperature -4 °C. Most particles near the melting level are ice (Fig. 15b at 14.88 UTC). Some light rain occurs near the surface at the eastern end of the morning flight (Fig. 15e at 15.04 UTC). During the afternoon flight (Fig. 16), the thin clouds were all primarily composed of liquid cloud droplets, and no precipitation was detected.

Rimed ice particles are encountered on the first ACB legs (14.25 UTC within Fig. 15b and 19.99 UTC within Fig. 16b) of both flights, at *in situ* temperatures of -6 to -7 °C, within thin clouds with a minimum T_{ct} near -8 °C. The high concentration of small super-cooled water droplets again suggests primary ice production is likely occurring at the same time as the cloud initiation. 2DS imagery throughout depicts super-cooled liquid water droplets and occasional large rimed ice particles and snow aggregates (e.g. at 14.75, 15.11 and 15.46 UTC) with no clear indication of diffusional growth. The highest N_i of 0.58 L^{-1} is sampled during a BCT leg at 15.8 UTC at a temperature of -10 °C. This implies a non-HM riming-splintering SIP mechanism. Rainrates remain light (0.1 mm hr^{-1} at best), and the significant cloud deepening to the east suggests the reduction in N_d is primarily occurring through cloud-top entrainment, rather than precipitation. MODIS imagery does not clearly suggest an open-celled structure at the end of either flight (Fig. 2), suggesting the transition to a lower-albedo cloud structure is primarily through continuing entrainment of warmer, drier air, with weakening surface boundary fluxes (Fig. 2) less able to couple the surface to the cloud layer.

e. 8 March 2021

Both planes traverse a narrower Gulf Stream three days later on 8 March 2021, during an afternoon-only flight (RF51). After transecting the Gulf Stream, the planes headed south-southwest to sample an area with broken clouds (Fig. 17). Near-surface winds are lighter (ERA5 wind speed maxima of 8 m s^{-1}) and buoyancy flux maxima remain < 400 W m^{-2} (Fig. 2). In contrast to the other flights, clouds do not develop until the boundary layer flow reaches the eastern GS edge and MODIS LWPs remain below 50 g m^{-2} in the area sampled by the planes.

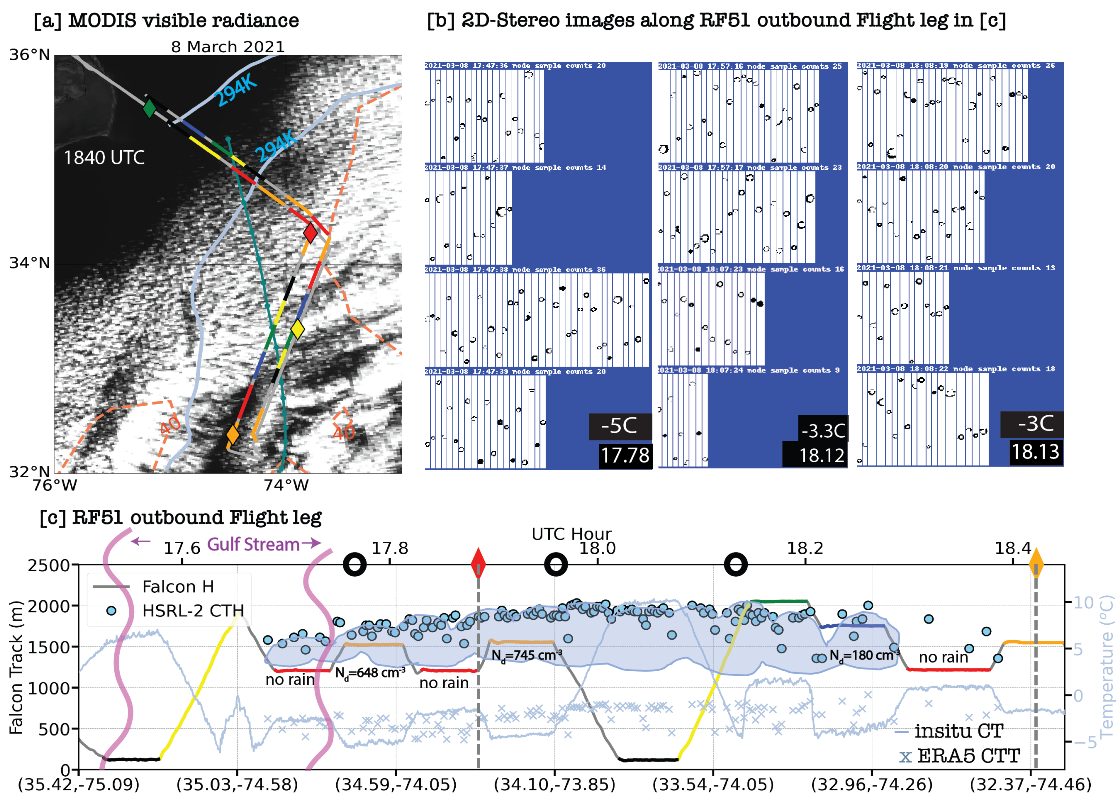

FIG. 17. 8 March 2021 afternoon flight (RF51). Ascent profiles shown in Fig. S7.

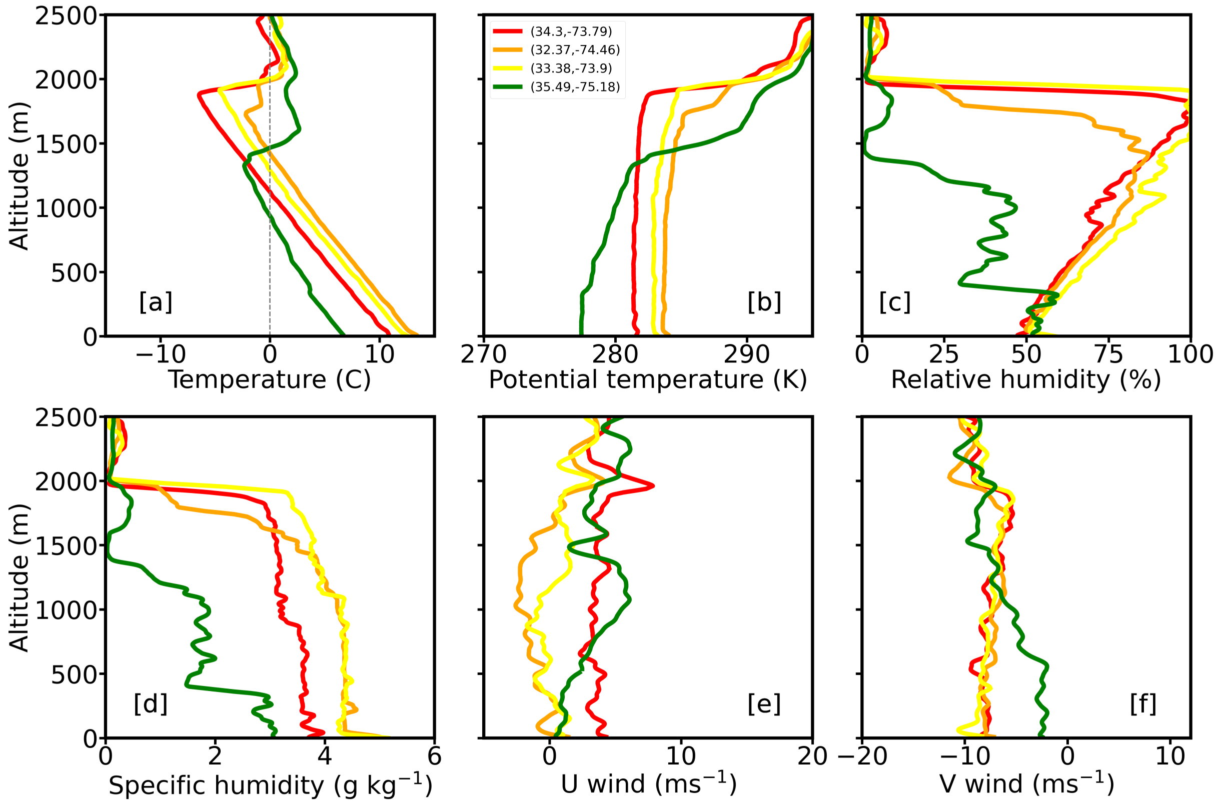

555 FIG. 18. 8 March 2021 (RF51) dropsonde profiles of a) temperature, b) potential temperature, c) relative
556 humidity, d) specific humidity, e) zonal wind and f) meridional winds. Colors follow those indicated within
557 diamonds in Fig. 17.

The dropsondes indicate the 0 °C level is already above one km at the western end of the flight before the clouds develop, under a capping temperature inversion at ~ 1.3 km (Fig. 18). The temperature inversion base deepens to near 2 km east of the Gulf Stream, and the 0 °C level and cloud base rise to between 1.1-1.5 km. No precipitation is detected below cloud base anywhere, indicating the ~50% reduction in N_d with fetch is primarily through cloud top entrainment. The coldest cloud temperatures only reach -5 °C. No particles were deemed aspherical enough to qualify as ice (see Fig. S5). However, on closer inspection, small mostly-spherical rimed ice particles are evident in the 2DS imagery at 18.12 and 18.13 UTC (Fig. 17b). The lidar ratio at 532 nm also indicates the presence of some ice. Ice particles have been detected at temperatures > -5 °C over the southern oceans (Zaremba et al. 2021), with this case suggesting ice in such warm conditions can also occur in these CAOs.

A roll circulation is suggested by the MODIS visible imagery, although the wind shear expected for a roll circulation (e.g., Young et al. 2002) is not present (Fig. 18d and e). Two dropsondes are located near each other, one within the clear area and the other sampling a nearby cloud (orange and yellow in Fig. 18). These have similar boundary layer specific humidities, with the clear-sky sounding being ~ 1 °C warmer, capped by a slightly lower inversion height than its neighbor. The buoyancy fluxes are also weaker (Fig. 2). Surface relative humidities remain near 50% for all four dropsondes, and the fluxes and updrafts may simply be too weak (Fig. 4) to bring near-surface air to its lifting condensation level, within the clear region. Mesoscale descent could additionally be acting to help dry and warm the cloud layer, as suggested for some CAOs within Chou and Ferguson (1991), and lower the inversion height. The cloud organization apparent in the visible imagery suggests this could be occurring, but this remains speculative without further analysis.

5. Evidence for Primary and Secondary ice production

Ice particles detected at the first pass through thin, developing cloud, just downstream of clear skies, in four of the examined cases indicates primary ice nucleation occurring at temperatures between -4 °C to -8 °C. This nucleation may be aided by strong updrafts. Marine boundary layer INP concentrations measured off the coast of eastern Nova Scotia ranged from 10^{-4} to 10^{-3} cm^{-3} (Irish et al. 2019; Welti et al. 2020). These exceed measured marine-originating INP concentrations over the Southern Oceans (McCluskey et al. 2018) and globally (DeMott et al.

2016), by 2-3 orders of magnitude at -15 °C. Electron microscopy identified the northwest Atlantic INP as mineral dust (Irish et al. 2019). INP concentrations during ACTIVATE CAOs can well be similarly elevated by outflow of continental soil aerosols. Welti et al. (2020) suggest the following estimate of primary ice nuclei concentrations based on a best-fit to multiple measurement datasets: INP=(T+5)*(-10^{-5}*exp(500/T+60)) with T in Celsius and INP in m^{-3}. This equation estimates an INP concentration of 1.1* 10^{-3} L^{-1} at -10 ° C, reducing to zero at -5 °C.

The empirical Welti et al. (2020) INP estimate is 1-2 orders of magnitude less than that in currently used parameterizations of INP. At -10 °C, the Meyers et al. (1997) contact nucleation formulation estimates INP of 0.3 L^{-1}. The deposition freezing parameterization of Cooper (1986) produces an INP estimate of 0.05 L^{-1}. The immersion freezing parameterization of Bigg (1953) produces lower concentrations, but overall, these parameterizations overestimate INPs relative to Welti et al. (2020). The parameterization overestimate is consistent with the known bias in cloud phase within global models, wherein ice depletes super-cooled water too quickly (e.g., Atlas et al. 2022).

Nevertheless, ice particle concentrations measured during the ACTIVATE CAOs cannot be explained by primary ice production alone. We compile the ice microphysical properties for the four ice-containing flights in Figs. 19-21 to help identify dominant production mechanisms for secondary ice production. *In-situ* temperatures of the ACB and BCT legs range between -12 °C to near 0 °C, with most occurring between -5 °C to -9 °C (Fig. 19). Measured N_i concentrations range from 0.1 L^{-1} to 5 L^{-1}, with the larger values found both near colder cloud tops (< -8 °C) and warmer ACB legs (Fig. 19). The N_i enhancement is consistent with other observations within convective clouds with cloud top temperatures warmer than -12 °C (Abel et al. 2017; Field et al. 2017; Järvinen et al. 2022). Notably, although many of the elevated N_i values fall within the HM temperature regime (-3 °C to -8 °C), the highest N_i concentrations mostly occur at either warmer or colder temperatures.

The distribution of IWC with temperature is also bimodal (Fig. 20a). IWCs are also higher for larger LWPs and larger cloud-top effective radius (both from MODIS; Fig. 20b and c), with a less clear relationship to the *in situ* r_e or temperature (not shown). The colder cloud tops correspond to thicker clouds with more liquid water (Fig. S8), and the highest ice water contents occur within the clouds with the coldest tops (Fig. S9). These reach temperatures that favor dendritic vapor-

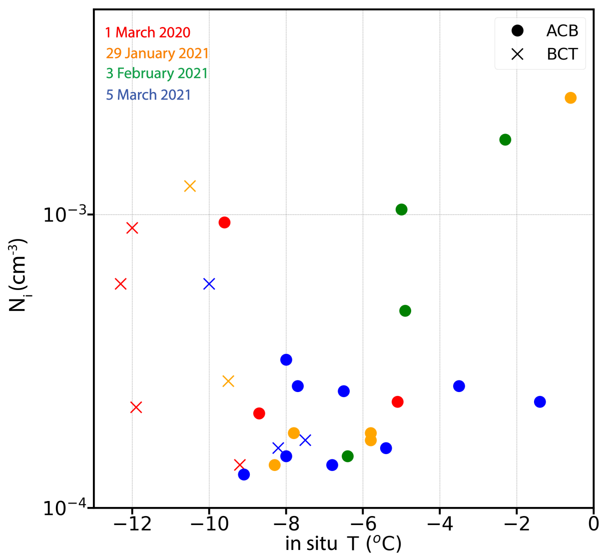

FIG. 19. Leg-mean *in-situ* N_i (one-second values > 0 only) versus temperature for the ACB (filled circles) and BCT (crosses) aircraft legs.

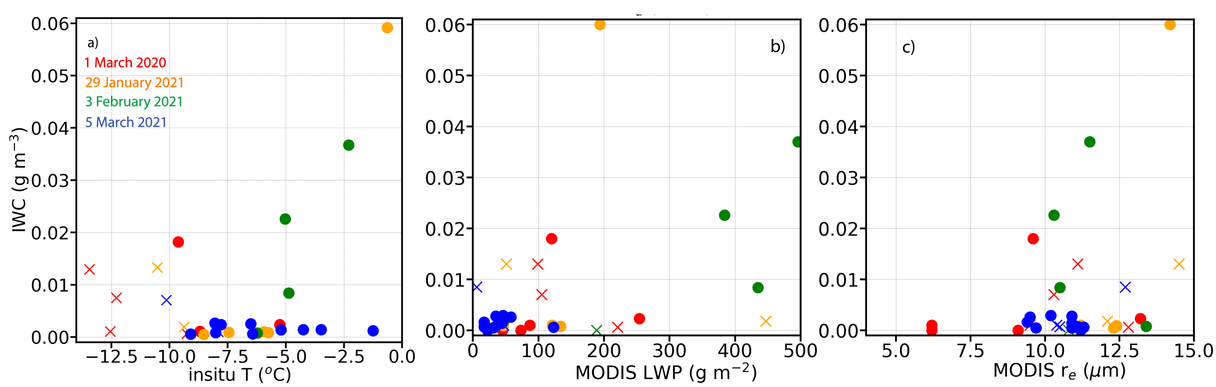

FIG. 20. Leg-mean *in-situ* IWC versus a) *in-situ* temperature, b) MODIS-derived LWP and c) effective radius (r_e), for above-cloud-base (ACB, filled circle) and below-cloud-top (BCT, crosses) aircraft legs. One-second $N_i$values > 0 only.

diffusional growth whose slower particle fall speeds allow more time for particle growth, also seen in the sub-Arctic (Chellini et al. 2022). Rainrates and rain fractions are larger for higher LWPs and colder T_{ct}s (Fig. 21).

The ice habits associated with the best-known SIP mechanism, riming followed by ice splintering at temperatures between -8 °C and -3 °C (Hallett and Mossop 1974), are columns, super-cooled liquid drops, and rimed particles are all evident within 2DS imagery for the 3 February 2021 case.

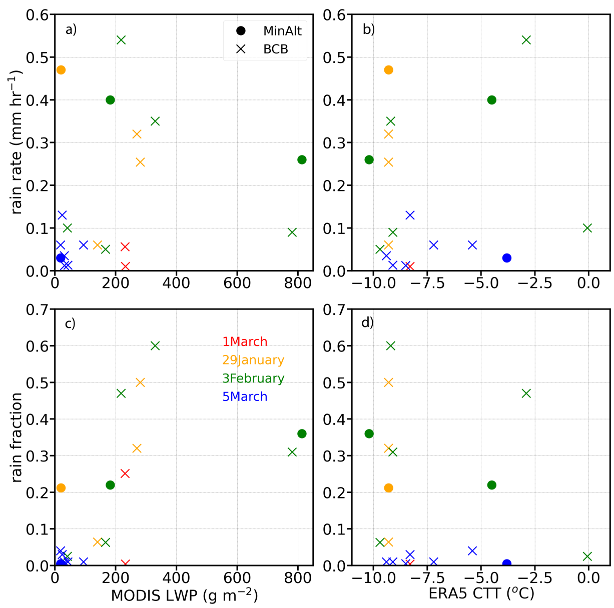

FIG. 21. *in situ* leg-mean rain rates versus a) MODIS LWP, b) ERA5 T_{ct}; leg-mean *in situ* rain fractions versus c) MODIS LWP and d) ERA5 T_{ct}. Rain rates and fractions based on one-second rain rates > 0.01 mm hr^{-1} only.

The HM mechanism is common in CAOs in the sub-Arctic region (Abel et al. 2017; Mages et al. 2023) and the southern oceans (Järvinen et al. 2022). That said, HM production of small ice columns is not always evident, notably within the strongest CAO occurring on 29 January, 2021. Instead, the largest N_i occur outside the HM temperature range (Fig. 19), and are often associated with higher IWCs. This suggests fragmentation after ice-ice particle collision, of either dendrites and/or graupel, is the more dominant SIP form. The graupel particles vary in size, which will also vary their fall speeds, a requirement for particle collisions. Ice-ice collisions generate ice splinters most effectively at temperatures ~ -16 °C (Takahashi et al. 1995), aided by the more fractal surfaces such as the snowflakes evident on 1 March 2020. Cloud top temperatures almost reach this temperature regime during the more intense CAOs (29 January and 3 February 2021). Positive correlations between N_i and IWC, such as on 29 January 2021 (Fig. 11), also occur on 1 March 2020 and 3 February 2021.

Because of the strength of the surface fluxes, 1 Hz updraft velocities at cloud base can easily reach 5 m s^{-1} (Fig. 4), in line with Mages et al. (2023). Closer to cloud top, the updrafts may also be able to bring some liquid droplets above the existing inversion, where they form an additional, thin, stratiform cloud layer under a new inversion, though horizontal inhomogeneities in cloud top height

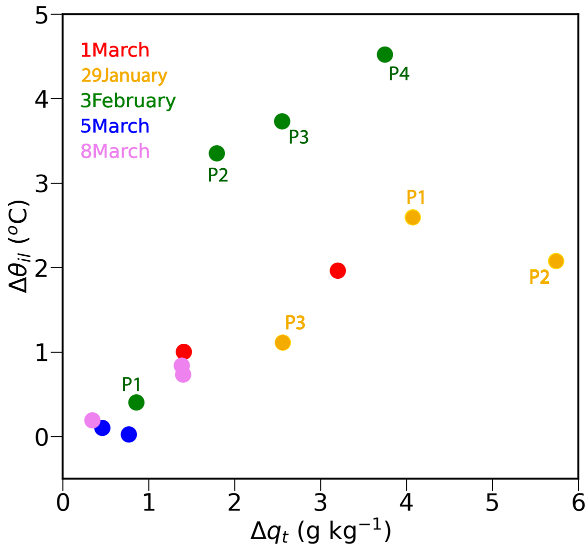

FIG. 22. Boundary layer decoupling metrics $\Delta\theta_{il}$ vs Δq_t. Profile labeling corresponds to that in Figs. 9-12 and Fig. 14.

can also explain this observation. A growing body of work is indicating that SIP is more likely to occur within updrafts (Luke et al. 2021; Mages et al. 2023), although a cursory examination did not reveal this for the cases examined here. This could be because the up/downdrafts also facilitate a recirculation of ice, constituting an internal feeder-seeder process. Deep strong updrafts are capable of lofting both graupel and generating super-cooled liquid droplets, and SIP is preferred near cloud top when both graupel and super-cooled liquid are present. Recirculation of ice may also facilitate a synergism across different SIP mechanisms (Sotiropoulou et al. 2020).

The strong updrafts, by increasing N_d and keeping drop sizes small, discourage attribution to the SIP mechanisms of droplet freezing and fragmentation during sublimation. Droplet fragmentation upon freezing (drop-shattering) is more effective for droplets with diameters > 100 μm (Korolev et al. 2020; Luke et al. 2021) and drizzle drops are few at the colder T_{ct}. High supersaturation within strong updrafts can also enhance INP activation. This may be occurring, but cloud temperatures are too warm for significant primary ice particle production. Fragmentation through sublimation also seems unlikely because the large number of super-cooled droplets will maintain a relative humidity near water-saturation.

a. Is precipitation-induced decoupling occurring?

Precipitation-induced decoupling is generally necessary to the transition to open-celled structures in subtropical marine stratocumulus (Wood et al. 2011), and is emphasized within Abel et al. (2017) for a sub-Arctic CAO cloud transition. We investigate boundary layer decoupling for the ACTIVATE CAOs using the metric developed within Jones et al. (2011), also applied within Abel et al. (2017). Differences between the upper ("top") and lower ("bottom") quarter of the boundary layer total water (ice+liquid+vapor mixing ratio; q_t) and the ice-liquid water potential temperature (θ_{il}) indicate the degree to which the cloud and sub-cloud layers are coupled. Profiles with Δq_t (= $q_{t,bottom} - q_{t,top}$) of 1.5 g kg^{-1} and $\Delta\theta_{il}$ (= $\Delta\theta_{il,top} - \theta_{il,bottom}$) of $\simeq 1\ ^\circ C$ in Fig. 22 are considered well-mixed. These apply primarily to 5 and 8 March 2021 and the most western profiles from 1 March 2020 and 3 February 2021. This further supports the idea that the CAO cloud fraction on 5 and 8 March 2021 eventually becomes reduced because buoyancy fluxes become too weak to support a cloudy boundary layer. Many of the other profiles possess more dramatic vertical gradients in q_t and θ_{il} than does the Abel et al. (2017) CAO, especially further east. The boundary layer on 3 February, which supports the largest rain rates and fractions of the 5 days, is the deepest and most decoupled in temperature. Precipitation is closely linked to decoupling for both 29 January and 3 February 2021. Thus although surface fluxes may overcome rain-induced cooling near the surface in places (e.g., Fig. 13), the lower quarter of the boundary layer is still only occasionally coupled to the cloud layer though cumulus. Interestingly, despite being decoupled, all of the 29 January 2021 profiles still correspond to overcast conditions, as does the P3 3 February 2021 profile. This is consistent with detrainment near cloud-top and serves to demonstrate how the bottom-up convection of cold-air outbreaks underneath a synoptically-induced inversion influences cloud fraction differently from the subtropical cloud decks.

6. Conclusions

As outbreaks of cold air flow off of the eastern north American continent in the boreal winter and spring over the cold Labrador current, and then over the warm Gulf Stream, strong surface fluxes of heat and moisture deepen the boundary layer, saturate its upper level with moisture and foster significant cloud development, over a distance of under 1000 km. The surface fluxes typically initiate cloud near the western edge of the Gulf Stream at $< 0\ ^\circ$C temperatures, developing reflective stratiform cloud decks that devolve into lower-albedo cloud structures as the flow moves past the eastern GS edge. Cloud tops rise to mostly remain at their initial temperature, ranging between -10 °C to -14 °C for the more intense CAOs, while the 0 °C level rises more dramatically, so that more and more of the cloud comes to occupy temperatures > 0°C.

The transition to lower-albedo cloud can occur via two pathways. In the five days examined here, the more intense CAOs, which typically occur earlier in the year (Painemal et al. 2023), deepen more and sustain both more ice and more rain by the eastern GS edge, than do the less intense CAOs occurring later in the year. In the limited sample size examined here, precipitation reaching the surface only sets in after the CAO has reached the eastern GS edge and beyond. Since super-cooled liquid exists throughout the vertical column, the precipitation reaching the surface could either be from melting snow or the collision-coalescence of liquid droplets. The presence of strong updrafts suggests graupel is likely the common precursor to the rain, however, consistent with space-based radar and lidar analysis (Field and Heymsfield 2015; Mülmenstadt et al. 2015). The rain facilitates the transition of the more intense CAOs (29 January and 3 February, 2021) to an open-celled organization. More intense CAOs are known to produce more extended high cloud fractions (Fletcher et al. 2016), and the high aerosol loadings should maintain the stratiform decks for longer (Murray-Watson et al. 2023), as is also observed in the satellite imagery shown here. In this study, thin cloud layers may be occurring above well-defined inversion bases (e.g., Fig. 6), because of the strong updrafts, though the layers may also correspond to detrainment from cloud tops at different heights. The cloud deepening and N_d depletion lag the SST increase (Tornow et al. 2021). These processes are encapsulated in Fig. 23. In the second pathway, the cloud breakup for the weaker CAOs (5 and 8 March 2021) is better explained by surface fluxes that become too weak to sustain cloud development within deeper boundary layers that have warmed with fetch. Mesoscale wind circulations generated either by the strong SST gradients (Small et al. 2008; Liu et al. 2014) or above-cloud-top wind shear (Young et al. 2002) may potentially impose imprints on the cloud organization, but this remains a topic for future research. We also note that for this regime, LWP and N_d are not anti-correlated as they are for other suppressed marine regions (Gryspeerdt et al. 2019).

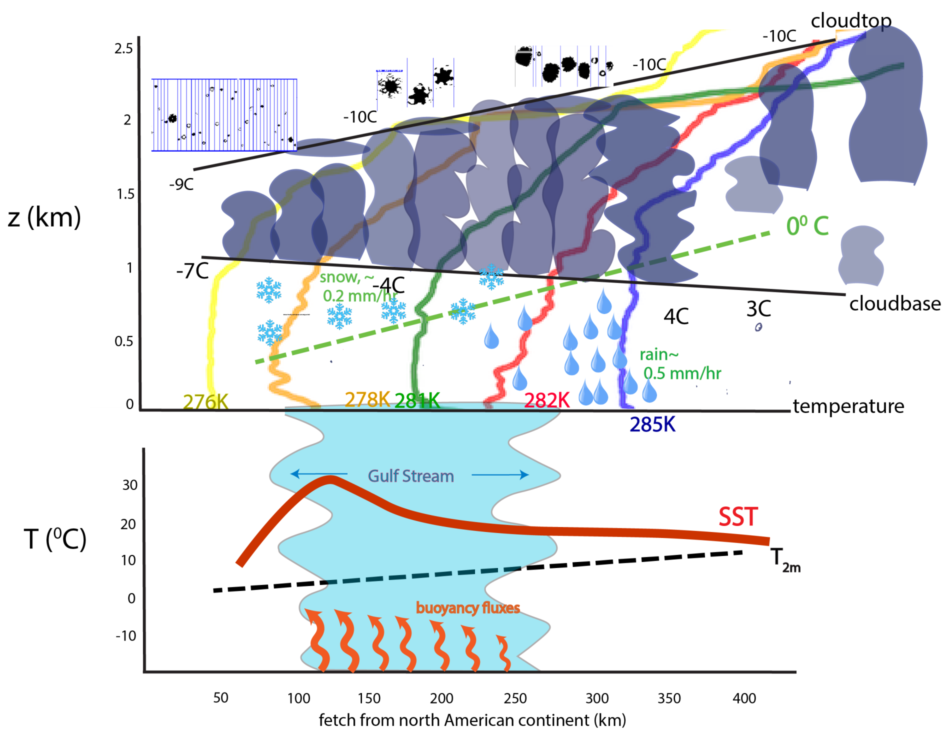

720 FIG. 23. Schematic depiction of main processes controlling the microphysical evolution of cold-air outbreaks
721 over the northwest Atlantic, including the dropsonde profiles of potential temperature from 3 February 2021.

Ice is already present even in thin, polluted clouds with small drops for which T_{ct} barely reaches -5 °C - -8 °C, even for the weakest, warmest, CAO. The proximity to clear-sky region upwind suggests that the primary ice nucleation occurs at the time of cloud initiation. We hypothesize the land-originating aerosol composition emanating off of the eastern seaboard already contains some ice-nucleating particles, similar to measurements above Baffin Bay (Irish et al. 2019), though marine emissions are also a possibility. Thereafter, rimed ice co-exists with small supercooled liquid drops, aided by updrafts reaching five m s^{-1}. In temperature ranges that favor dendritic growth, snowflakes are also apparent (e.g. 1 March 2020). Elevated ice number concentrations, outside of the Hallett-Mossop temperature range, contribute to a growing body of evidence for other SIP mechanisms at temperatures warmer than -15 °C (Zaremba et al. 2021; Järvinen et al. 2022). N_i are highest near cloud top and near cloud base and correlate with IWC for the three more intense CAOs. Elevated IWCs near 0 °C indicates enhanced ice aggregation. Although the 2DS imagery is not definitive, ice-ice (including graupel) collisions, favored in temperature ranges that support dendritic growth and enhanced ice aggregation, is hypothesized to produce the secondary ice. SIP occurs outside the HM temperature range on 29 January 2021, while four days later on 3 February 2021, HM rime-splintering is evident in ice columns. This suggests multiple SIP pathways can readily occur, similar to the sub-Arctic (Sotiropoulou et al. 2020; Karalis et al. 2022) and over the southern Oceans (Järvinen et al. 2022; Atlas et al. 2022). Small dropsizes should discourage droplet freezing, all else equal, with the strong up- and downdrafts facilitating recirculation of ice that may further promote ice production.

The cold-air outbreaks examined here differ from those in the sub-Arctic and southern Ocean in part by being more polluted (Dadashazar et al. 2021), increasing the N_d to values > 500 cm^{-3} on the western side of the Gulf Stream. In addition, the SST gradients are more pronounced than over the sub-Arctic, supporting surface fluxes and updrafts that can reach above 500 W m^{-2} and five m s^{-1} (contrast with surface fluxes and updrafts that remained below 200 W m^{-2} and two m s^{-1} in Young et al. (2016), Abel et al. (2017) and Duscha et al. (2022)). Further work remains to be done. Several of these cases lend themselves well to a follow-up study that can better differentiate cause and effects. Dynamical effects from mesoscale circulations induced either by the strong SST gradients and/or wind shear remain unexplored. In addition, a future study evaluating the full dataset of available profiles will be required to better assess the various remote sensor retrievals in these mixed-phase conditions.

Acknowledgments. We gratefully acknowledge funding support through grant 80NSSC19K0390 to University of Miami and grant no. 80NSSC19K0442 to University of Arizona. Christiane Voigt and Simon Kirschler were funded by the Deutsche Forschungsgemeinschaft (DFG, German Research Foundation – TRR 301 – Project ID 428312742 and SPP 1294 HALO under contract no. VO 1504/79-1). We thank Kevin Sanchez and Alexei Korolev for their insights into cloud probe behavior and microphysical behavior. The NASA Earth Venture Suborbital-3 Aerosol Cloud meTeorology Interactions Ver the western ATlantic Experiment (ACTIVATE) campaign was funded by NASA's Earth Science Division and managed through the Earth System Science Pathfinder Program Office.

Data availability statement. All ACTIVATE datasets are available through ASDC: Atmospheric Science Data Center [data set], `https://doi.org/10.5067/SUBORBITAL/ACTIVATE/DATA001`, 2020.

APPENDIX A

Assessment of *in situ* and remotely-retrieved cloud properties

A complete assessment of the 'best-estimate' N_d values from either the probes or the RSP is beyond the scope of this work, but here we provide a preliminary analysis. CDP N_d values are typically smaller than those from the FCDP, perhaps because of coincidence undercounting, wherein two or more particles simultaneously travel through a sample volume but are counted as one, and because of differences in the effective flow speed of $\sim$ 15%. The effective radius (r_e) values are similar between the two probes for 2020 data, indicating the N_d difference is primarily an undercounting at all sizes. An empirical correction based on 2020 data is applied: $N_{d,CDP_{corr}}$= α (e$^{(\beta * N_{d,CDP})}$ -1), with α=1820 and β =6.9e-4 (Kevin Sanchez, personal communication). This closely follows the Lance (2012) correction. The corrected CDP N_d values exceed the FCDP values on average in 2020 (mean ratio of 1.9), but are 70% of the FCDP values in 2021 on average.

Small changes in voltage can also dramatically change the number of droplets meeting the 3 μm diameter threshold of the FCDP, however. The FCDP N_d concentrations are typically only slightly less than the CCN concentrations measured at 0.3-0.4 % supersaturation (Fig. A1a) based on just the data from the five investigated flight days. The CDP N_d values show a relationship to the CCN that is more typical of marine environments. The FCDP N_d values, while high, are nevertheless

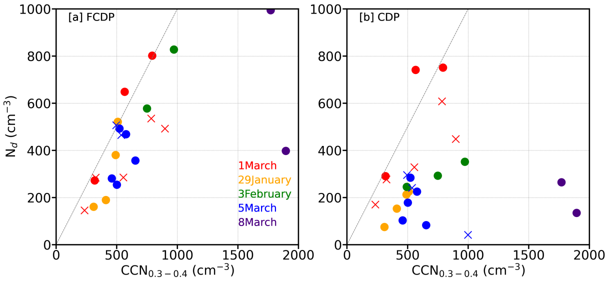

Fig. A1. Cloud droplet number concentrations (N_d) versus cloud condensation nuclei concentration (CCN) measured at 0.3-0.4% supersaturation, taken from level legs occurring below one km in altitude gridded to one-degree, for a) FCDP and b) the corrected CDP data.

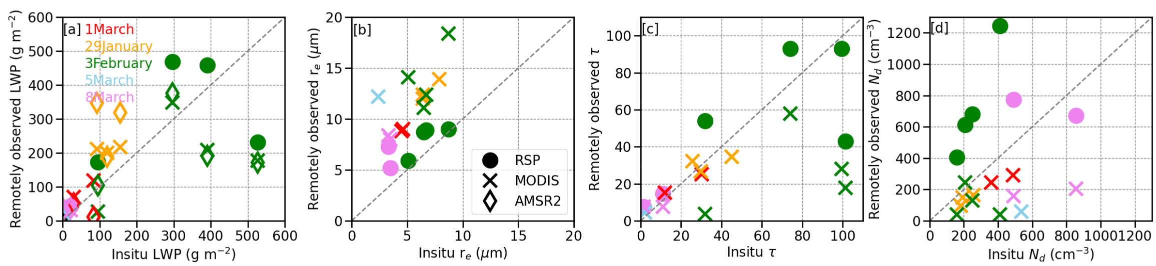

Fig. A2. RSP (filled circles) and MODIS (crosses) retrievals versus *in-situ* values of a) LWP, includes microwave-derived AMSR2-diamond, b) cloud-top effective radius r_e, c) cloud optical depth τ, and d) cloud droplet number concentration N_d. Flight day is indicated by color. RSP data are screened for the presence of higher clouds.

possible for a regime with strong surface fluxes, and which may contain further aerosol capable of becoming activated at higher supersaturations.

The available remotely-retrieved (RSP, MODIS, and AMSR2) cloud properties are also compared to those calculated from the available *in situ* profiles, for both the FCDP probe (Fig. A2) and the CDP probe (Fig. A3), and, for the RSP, shown along the 3 February 2021 flight track with the CDP r_e values (Fig. A4). The RSP retrieves the r_e and cloud optical depth τ using multi-angle polarized radiances at the cloud bow, primarily at the 865 nm wavelength. The radiances are dominated by single scattering and little impacted by three-dimensional radiative transfer effects (Alexandrov et al. 2012, 2015). The field of view is 14 mrad, and the data are aggregated into a one-second resolution, corresponding to a $\sim$ 100 m spatial resolution, oriented along the aircraft track, then averaged further into one-minute moving averages in Fig. A4.

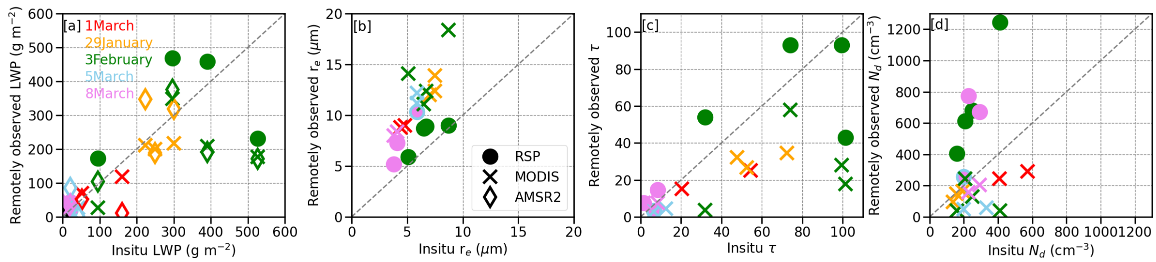

FIG. A3. similar to Fig. A1 but for the CDP probe values.

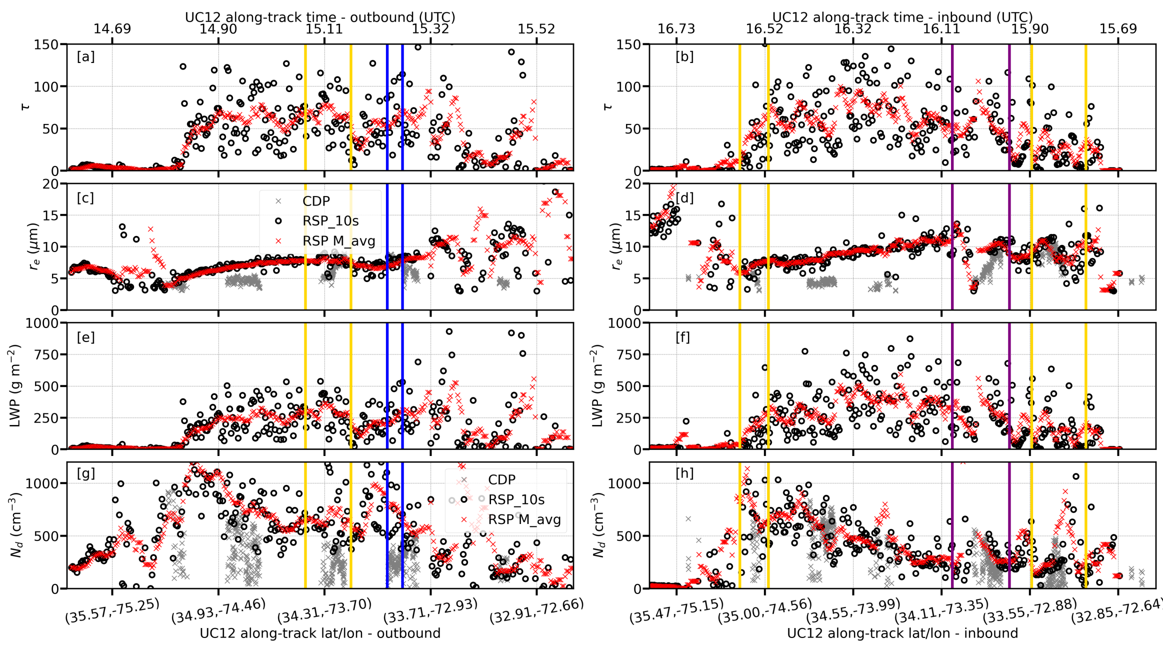

FIG. A4. a) RSP-derived cloud optical depths along outbound flight track of 3 February 2021 morning flight (RF44), from west to east, as ten-second and moving one-minute averages (black open circles and red asterisks, respectively). b) same as a) but for inbound (return) flight, west to east. c)-d): same as a)-b) but for RSP-derived r_e and that from the CDP probe where available (grey asterisks). e)-f): RSP-derived LWP. g)-h) RSP-derived N_d and that from the CDP probe where available (grey asterisks). Yellow/purple lines bracket ascent/descent profiles and dark blue indicates the BCT leg.

The RSP r_e is typically within two μm of the *in situ* values near cloud top, lending confidence to both measurements (Fig. A2b and Fig. A3b). In Fig. A4e-f, the RSP r_e slightly exceeds the *in situ* values from lower in the cloud, as expected. The strong correspondence between the RSP and *in situ* cloud-top r_e is supported by a larger-scale assessment of ACTIVATE data (not shown), comparisons to Langley CDP data over the northern Atlantic (Alexandrov et al. 2018), and from another cloud probe over the southeast Atlantic (Adebiyi et al. 2020).

The *in-situ* τ values are summed over a profile of regridded, 20-m vertical-mean volume extinction coefficients ($\beta(z)$) calculated from LWCs and effective radii ($r_e(z)$) as $\beta(z) = \frac{9LWC}{5\rho_w r_e(z)}$. The factor of $\frac{9}{5}$ accounts for an adiabatic increase in LWC over the 20-m span, supported by the profiles. For the six *in situ* profiles for which RSP retrievals are also available, the RSP cloud optical depths values seem representative. LWP is estimated using $\frac{5}{9}\rho_w \tau r_e$, where r_e is the cloud-top value. Differences from *in situ* LWP values are dominated by the differences in τ. RSP retrievals of N_d, calculated using $N_d = k\frac{\tau^{0.5}}{r_e^{2.5}}$ with k=1.4067 x 10^{-6} [cm$^{-0.5}$] following Painemal and Zuidema (2011) typically exceed vertically-averaged *in situ* values, similar to Gryspeerdt et al. (2022). This does reflect vertical inhomogeneity in the *in situ* values in part. Along the 3 February 2021 flight track, the RSP-derived N_d are close to the maximum *in situ* N_d values (Fig. A4g-h), reaching 1000 cm^{-3} in places, while retrieved LWPs mostly remain 500 g m^{-2}. These comparisons tend to support each other.

MODIS r_e values, retrieved at 3.7 μm, typically exceed *in situ* values (see also Fig. S7), consistent with other comparisons (e.g., Painemal and Zuidema 2011; Painemal et al. 2021). MODIS τ estimates are consistently less than *in situ* values, likely because of unaccounted-for horizontal photon transport (Zuidema and Evans 1998). The MODIS biases in τ and r_e somewhat compensate each other within the LWP estimate, but nevertheless remain less than RSP-derived LWPs (Figs. A2a-A3a). This is in large part due to the resolution difference between RSP and MODIS (100 m versus 1 km). When RSP radiances are averaged, using a one-minute moving average which gives a spatial average similar to MODIS resolution, and LWP retrieved from the one-minute radiance values, the LWP is 60%-70% of that obtained using a one-minute moving average of the LWP retrieved at the native resolution. Fully-independent Advanced Microwave Scanning Radiometer-2 (AMSR2) satellite measurements of LWP appear closer to the *in-situ* values in Figs. A2a and A3a, but this may be fortuitous, as the time differences are also larger. MODIS N_d values are consistently less than the vertically-averaged *in situ* values, also seen in (Gryspeerdt et al. 2022). We speculate this is because of the strong dependence on the r_e retrieval.

References

Abel, S. J., I. A. Boutle, K. Waite, S. Fox, P. R. Brown, and R. C. et al., 2017: The role of precipitation in controlling the transition from stratocumulus to cumulus clouds in a northern hemisphere cold-air outbreak. *J. Atmos. Sci.*, **74**, 2293–2314, https://doi.org/10.1175/jas-d-16-0362.1.

Adebiyi, A. A., P. Zuidema, I. Chang, S. P. Burton, and B. Cairns, 2020: Mid-level clouds are frequent above the southeast atlantic stratocumulus clouds. *Atmos. Chem. Phys.*, **20**, 11 025–11 043, https://doi.org/10.5194/acp-20-11025-2020.

Alexandrov, M., B. Cairns, A. Wasilewski, A. Ackerman, M. McGill, and e. a. J. Yorks, J., 2015: Liquid water cloud properties during the polarimeter definition experiment (PODEX). *Rem. Sens. Env.*, **169**, 20–36.

Alexandrov, M. D., B. Cairns, C. Emde, A. S. Ackerman, and B. van Diedenhoven, 2012: Accuracy assessments of cloud droplet size retrievals from polarized reflectance measurements by the research scanning polarimeter. *Rem. Sens. Env.*, **125**, 92–111.

Alexandrov, M. D., and Coauthors, 2018: Retrievals of cloud droplet size from the research scanning polarimeter data: Validation using in situ measurements. *Remote Sens. Environ.*, **210**, 76–95, https://doi.org/10.1016/j.rse.2018.03.005.

Atlas, R. L., C. S. Bretherton, M. F. Khairoutdinov, and P. N. Blossey, 2022: Hallett-mossop rime splintering dims cumulus clouds over the southern ocean: New insight from nudged global storm-resolving simulations. *AGU Advances*, **3**, https://doi.org/10.1029/2021AV000454.

Bigg, E. K., 1953: The supercooling of water. *Proc. Phys. Soc.*, **66B**, 688–694, https://doi.org/10.1088/0370-1301/66/8/309.

Bodas-Salcedo, A., and Coauthors, 2014: Origins of the solar radiation biases over the southern ocean in CFMIP2 models. *J. Clim.*, **27**, 41– 56, https://doi.org/10.1175/JCLI-D-13-00169.1.

Chellini, G., R. R. Gierens, and S. Kneifel, 2022: Ice aggregation in low-level mixed-phase clouds at a high Arctic site: Enhanced by dendritic growth and absent close to the melting level. *J. Geophys. Res.*, **127**.

Chou, S. H., and M. P. Ferguson, 1991: Heat fluxes and roll circulations over the western Gulf Stream during an intense cold-air outbreak. *Bound.-Layer Meteor.*, **55**, 255–281.

Choularton, T. W., D. J. Griggs, B. Y. Humood, and J. Latham, 1980: Laboratory studies of riming, and its relation to ice splinter production. *Q. J. Roy. Meteor. Soc.*, **106**, 367–374, https://doi.org/10.1002/qj.49710644809.

Christensen, M. W., W. K. Jones, and P. Stier, 2020: Aerosols enhance cloud lifetime and brightness along the stratus-to-cumulus transition. *PNAS*, **117**, 17,591–17,598, https://doi.org/10.1073/pnas.1921231117.

Cooper, W. A., 1986: Ice initiation in natural clouds. *Precipitation Enhancement—A Scientific Challenge, Meteor. Monogr.*, 29–32.

Corral, A. F., and Coauthors, 2021: An overview of atmospheric features over the Western North Atlantic Ocean and North American East Coast – Part 1: Analysis of aerosols, gases, and wet deposition chemistry. *J. Geophys. Res.*, **126**, https://doi.org/10.1029/2020JD032592.

Dadashazar, H., and Coauthors, 2021: Cloud drop number concentrations over the western north atlantic ocean: Seasonal cycle, aerosol interrelationships, and other influential factors. *Atmos. Chem. Phys.*, **21**, 10 499–10 526, https://doi.org/10.5194/acp-21-10499-2021.

DeMott, P. J., T. Hill, C. McCluskey, K. Prather, D. Collins, and R. S. et al., 2016: Sea spray aerosol as a unique source of ice nucleating particles. *PNAS*, **113**, 5797–5803.

Dirks, R., J. P. Kuettner, and J. A. Moore, 1988: Genesis of Atlantic Lows Experiment (GALE): An Overview. *Bull. Amer. Meteorol. Soc.*, **69**, 148–160.

Duscha, C., C. Barrell, I. A. Renfrew, I. Brooks, H. Sodemann, and J. Reuder, 2022: A ship-based characterization of coherent boundary-layer structures over the lifecycle of a marine cold-air outbreak. *Bound.-Layer Meteor.*, **183**, 355–380.

Eirund, G. K., U. Lohmann, and A. Possner, 2019: Cloud ice processes enhance spatial scales of organization in arctic stratocumulus. *Geophys. Res. Lett.*, **46**, 14,109–14,117.

Fabry, F., and I. Zawadzki, 1995: Long-term radar observations of the melting layer of precipitation and their interpretation. *J. Atmos. Sci.*, **52**, 838–851.

Ferrare, R., and Coauthors, 2023: Airborne HSRL-2 measurements of elevated aerosol depolarization associated with nonspherical sea salt. *Front. Rem. Sens.*, **4**, https://doi.org/10.3389/frsen.2023.1143944.

Field, P. R., and A. J. Heymsfield, 2015: Importance of snow to global precipitation. *Geophys. Res. Lett.*, **42**, 9512–9520, https://doi.org/10.1002/2015GL065497.

Field, P. R., and Coauthors, 2017: Exploring the convective grey zone with regional simulations of a cold air outbreak. *Q.J.R. Meteorol. Soc*, **143**, 2537–2555, https://doi.org/10.1002/qj.3105.

Fletcher, J. K., S. L. Mason, and C. Jakob, 2016: A climatology of clouds in marine cold air outbreaks in both hemispheres. *J. Climate*, **29**, 6677–6692, https://doi.org/10.1175/JCLI-D-15-0783.1.

Frey, W. R., A. L. Morrison, J. E. Kay, R. Guzman, and H. Chepfer, 2018: The combined influence of observed southern ocean clouds and sea ice ontop-of-atmosphere albedo. *J. Geophys. Res.*, **123**, 4461–4475, https://doi.org/10.1029/2018JD028505.

Geerts, B., and Coauthors, 2022: The COMBLE Campaign: A Study of Marine Boundary Layer Clouds in Arctic Cold-Air Outbreaks. *Bull. Am. Meteor. Soc.*, **103 (5)**, E1371 – E1389, https://doi.org/10.1175/BAMS-D-21-0044.1.

Gettelman, A., and Coauthors, 2010: Global simulations of ice nucleation and ice supersaturation with an improved cloud scheme in the Community Atmosphere Model. *J. Geophys. Res.*, **115**.

Gryspeerdt, E., and Coauthors, 2019: Constraining the aerosol influence on cloud liquid water path. *Atmos. Chem. Phys.*, **19**, 5331–5347.

Gryspeerdt, E., and Coauthors, 2022: The impact of sampling strategy on the cloud droplet number concentration estimated from satellite data. *Atmos. Meas. Tech.*, **15**, 3875–3892, https://doi.org/10.5194/amt-15-3875-2022.

Hallett, J., and S. C. Mossop, 1974: Production of secondary ice particles during the riming process. *Nature*, **249**, 26–28, https://doi.org/10.1038/249026a0.

Hu, Y., and Coauthors, 2009: CALIPSO/CALIOP Cloud Phase Discrimination Algorithm. *J. Atmos. and Ocean. Tech.*, **26**, 2293–2309, https://doi.org/https://doi.org/10.1175/2009JTECHA1280.1.

Irish, V. E., and Coauthors, 2019: Ice nucleating particles in the marine boundary layer in the canadian arctic during summer 2014. *Atmos. Chem. Phys.*, **19**, 1027–1039.

Jones, C. R., C. S. Bretherton, and D. Leon, 2011: Coupled vs. decoupled boundary layers in VOCALS-REx. *Atmos. Chem. Phys.*, 7143–7153, https://doi.org/10.5194/acp-11-7143-2011.

Järvinen, E., and Coauthors, 2022: Evidence for secondary ice production in southern ocean maritime boundary layer clouds. *J. Geophys. Res.*, **127**.

Karalis, M., G. Sotiropoulou, S. J. Abel, E. Bossioli, P. Georgakaki, G. Methymaki, A. Nenes, and M. Tombrou, 2022: Effects of secondary ice processes on a stratocumulus to cumulus transition during a cold-air outbreak. *Atmos. Res.*, **277**, https://doi.org/https://doi.org/10.1016/j.atmosres.2022.106302.

Kirschler, S., and Coauthors, 2022: Seasonal updraft speeds change cloud droplet number concentrations in low-level clouds over the western north atlantic. *Atmos. Chem. Phys.*, **22**, 8299–8319, https://doi.org/10.5194/acp-22-8299-2022.

Kirschler, S., and Coauthors, 2023: Overview and statistical analysis of boundary layer clouds and precipitation over the western north-atlantic ocean. *Atmos. Chem. Phys. Disc.*, https://doi.org/10.5194/egusphere-2023-898.

Korolev, A., and Coauthors, 2020: A new look at the environmental conditions favorable to secondary ice production. *Atmos. Chem. Phys.*, **20**, 1391–1429, https://doi.org/10.5194/acp-20-1391-2020.

Lance, S., 2012: Coincidence errors in a Cloud Droplet Probe (CDP) and a Cloud and Aerosol Spectrometer (CAS), and the Improved Performance of a Modified CDP. *J. Atmos. Oceanic Tech.*, **29**, 1532–1541, https://doi.org/10.1175/JTECH-D-11-00208.1.

Lauber, A., A. Kiselev, T. Pander, P. Handmann, and T. Leisner, 2018: Secondary ice formation during freezing of levitated droplets. *J. Atmos. Sci.*, **75**, 2815–2826.

Lawson, P., and P. Zuidema, 2009: Aircraft microphysical and surface-based radar observations of summertime arctic clouds. *J. Atmos. Sci.*, **66**, 3505–3529, https://doi.org/10.1175/2009JAS3177.1.

Liu, J., S. Xie, J. R. Norris, and S. Zhang, 2014: Low-level cloud response to the gulf stream front in winter using CALIPSO. *J. Clim.*, **27**, 4421–4432.

Luke, E. P., F. Yang, P. Kollias, A. Vogelmann, and M. Maahn, 2021: New insights into ice multiplication using remote-sensing observations of slightly supercooled mixedphase clouds in the arctic. *Proc. Natl. Acad. Sci.*, **118**, https://doi.org/10.1073/pnas.2021387118.

Mages, Z., P. Kollias, Z. Zhu, and E. P. Luke, 2023: Surface-based observations of cold-air outbreak clouds during the COMBLE field campaign. *Atmos. Chem. Phys.*, **23**, 3561–3574, https://doi.org/10.5194/acp-23-3561-2023.

Matus, A. V., and T. S. L'Ecuyer, 2017: The role of cloud phase in earth's radiation budget. *J. Geophys. Res.*, **122**, 2559–2578, https://doi.org/10.1002/2016JD025951.

McCluskey, C. S., T. C. Hill, R. Humphries, A. Rauker, S. Moreau, and P. S. et al., 2018: Observations of ice nucleating particles over southern ocean waters. *Geophys. Res. Lett.*, **45**, 11 989–11 997, https://doi.org/10.1029/2018GL079981.

McFarquhar, G. M., C. S. Bretherton, R. Marchand, A. Protat, P. DeMott, and S. A. et al., 2021: Observations of clouds, aerosols, precipitation, and surface radiation over the southern ocean: An overview of CAPRICORN, MARCUS, MICRE and SOCRATES. *Bull. Am. Meteor. Soc.*, **102**, E894–E928, https://doi.org/10.1175/bams-d-20-0132.1.

McGraw, Z., T. Strovelmo, L. Polvani, S. Hofer, J. Shaw, and A. Gettelman, 2023: On the links between ice nucleation, cloud phase and climate sensitivity in CESM2. *Geophys. Res. Lett.*, **123**.

Meyers, M. P., R. L. Walko, J. Y. Harrington, and W. R. Cotton, 1997: New RAMS cloud microphysics parameterization. Part II: The two-moment scheme. *Atmos. Res.*, **45**, 3–39.

Milbrandt, J. A., and H. Morrison, 2016: Parameterization of cloud microphysics based on the prediction of bulk ice particle properties. part iii: Introduction of multiple free categories. *J. Atmos. Sci.*, **73**, 975–995.

Minobe, S., A. Kuwano-Yoshida, and N. K. et al., 2008: Influence of the gulf stream on the troposphere. *Nature*, **452**, 206–209, https://doi.org/10.1038/nature06690.

Mitchell, J. F. B., C. A. Senior, and W. J. Ingram, 1989: C02 and climate: A missing feedback? *Nature*, **341**, https://doi.org/10.1038/341132a0.

Mossop, S. C., 1976: Production of secondary ice particles during the growth of graupel by riming. *Quart. J. Met. Soc.*, **102**, 45–47.

Mülmenstadt, J., O. Sourdeval, J. Delano, and J. Quaas, 2015: Frequency of occurrence of rain from liquid-, mixed-, and ice-phase clouds derived from A-Train satellite retrievals. *Geophys. Res. Lett.*, **42**, 6502–6509, https://doi.org/10.1002/2015GL064604.

Murray-Watson, R. J., E. Gryspeerdt, and T. Goren, 2023: Investigating the development of clouds within marine cold air outbreaks. *Atmos. Chem. Phys. Disc.*

Naud, C. M., J. F. Booth, K. Lamer, R. Marchand, A. Protat, and G. McFarquhar, 2020: On the relationship between the marine cold air outbreak m parameter and low-level cloud heights in the midlatitudes. *J. Geophys. Res.*, **125**, https://doi.org/10.1029/2020JD032465.

Painemal, D., and P. Zuidema, 2011: Assessment of MODIS cloud effective radius and optical thickness retrievals over the Southeast Pacific with VOCALS-REx in-situ measurements. *J. Geophys. Res.*, **116**, https://doi.org/10.1029/2011JD016155.

Painemal, D., and Coauthors, 2021: Evaluation of satellite retrievals of liquid clouds from the GOES-13 imager and MODIS over the midlatitude North Atlantic during the NAAMES campaign. *Atmos. Meas. Tech.*, **14**, 6633–6646.

Painemal, D., and Coauthors, 2023: Wintertime synoptic patterns of variability of midlatitude boundary layer clouds over the western North Atlantic: Climatology and insights from in-situ ACTIVATE observations. *J. Geophys. Res.*, https://doi.org/10.1029/2022JD037725.

Papritz, L., S. Pfahl, H. Sodemann, and H. Wernli, 2015: A climatology of cold air outbreaks and their impact on air–sea heat fluxes in the high-latitude south pacific. *J. Climate*, **28**, 342–364, https://doi.org/10.1175/JCLI-D-14-00482.1.

Plagge, A., J. B. Edson, and D. Vandemark, 2016: In situ and satellite evaluation of air–sea flux variation near ocean temperature gradients. *J. Climate*, **29**, 1583–1602, https://doi.org/10.1175/jcli-d-15-0489.1.

Seethala, C., and Coauthors, 2021: On assessing ERA5 and MERRA2 representations of cold-air outbreaks across the Gulf Stream. *Geophys. Res. Lett.*, **48**, https://doi.org/10.1029/2021GL094364.

Small, R. J., S. P. deSzoeke, S. P. Xie, L. O'Neill, H. Seo, and Q. e. a. Q. Song, 2008: Air-sea interaction over ocean fronts and eddies. *Dynamics of Atmospheres and Oceans*, **45**, 274–319, https://doi.org/10.1016/j.dynatmoce.2008.01.001.

Sorooshian, A., and Coauthors, 2019: Aerosol-Cloud-Meteorology Interaction Airborne Field Investigations: Using lessons learned from the US west coast in the design of ACTIVATE off the east coast. *Bull. Am. Meteor. Soc.*, **100**, 1512–1528, https://doi.org/10.1175/BAMS-D-18-0100.1.

Sorooshian, A., and Coauthors, 2023: Spatially-coordinated airborne data and complementary products for aerosol, gas, cloud, and meteorological studies: The NASA ACTIVATE dataset. *Earth Sys. Sci. Data*, https://doi.org/10.5194/essd-2023-109.

Sotiropoulou, G., S. Sullivan, J. Savre, G. Lloyd, T. Lachlan-Cope, A. Ekman, and A. Nenes, 2020: The impact of secondary ice production on Arctic stratocumulus. *Atmos. Chem. Phys.*, **20**, 1301–1316, https://doi.org/10.5194/acp-20-1301-2020.

Takahashi, T., Y. Nagao, and Y. Kushiyama, 1995: Possible high ice particle production during graupel–graupel collisions. *J. Atmos. Sci.*, **52**, 4523–4527, https://doi.org/10.1175/1520-0469.

Tan, I., T. Storelvmo, and M. D. Zelinka, 2016: Observational constraints on mixed-phase clouds imply higher climate sensitivity. *Science*, **352**, 224–227.

Terai, C. R., Y. Zhang, S. A. Klein, M. D. Zelinka, J. C. Chiu, and Q. Min, 2019: Mechanisms behind the extratropical stratiform low-cloud optical depth response to temperature in ARM site observations. *J. Geophys. Res.*, **124**, 2127–2147.

Thornhill, K. L., B. E. Anderson, J. Barrick, D. Bagwell, R. Friesen, and D. Lenschow, 2003: Air motion intercomparison flights during Transport and Chemical Evolution in the Pacific (TRACE-P)/ACE-ASIA. *J. Geophys. Res.*, **108**, https://doi.org/10.1029/2002JD003108.

Tornow, F., A. S. Ackerman, and A. M. Fridlind, 2021: Preconditioning of overcast-to-broken cloud transitions by riming in marine cold air outbreaks. *Atmos. Chem. Phys.*, **21**, 12 049–12 067.

Tornow, F., and Coauthors, 2022: Dilution of boundary layer cloud condensation nucleus concentrations by free tropospheric entrainment during marine cold air outbreaks. *Geophys. Res. Lett.*, **49**, https://doi.org/10.1029/2022GL098444.

Vaillant de Guélis, T., A. Schwarzenböck, V. Shcherbakov, C. Gourbeyre, B. Laurent, R. Dupuy, P. Coutris, and C. Duroure, 2019: Study of the diffraction pattern of cloud particles and the respective responses of optical array probes. *Atmos. Meas. Tech.*, **12**, 2513–2529, https://doi.org/10.5194/amt-12-2513-2019.

Vömel, H., A. Sorooshian, C. Robinson, T. J. Shingler, K. L. Thornhill, and L. D. Ziemba, 2023: Dropsonde observations during the Aerosol Cloud meTeorology Interactions oVer the western ATlantic Experiment. *Scientific Data*, https://doi.org/10.1038/s41597-023-02647-5.

Wall, C. J., T. Storelvmo, J. R. Norris, and I. Tan, 2022: Observational constraints on southern ocean cloud-phase feedback. *J. Clim.*, **35**, 5087–5102.

Welti, A., and Coauthors, 2020: Ship-based measurements of ice nuclei concentrations over the arctic, atlantic, pacific and southern oceans. *Atmos. Chem. Phys.*, **20**, 15 191–15 206.

Wendisch, M., and Coauthors, 2019: The arctic cloud puzzle: Using acloud/pascal multiplatform observations to unravel the role of clouds and aerosol particles in arctic amplification. *Bull. Am. Meteor. Soc.*, **100 (5)**, 841 – 871, https://doi.org/10.1175/BAMS-D-18-0072.1.

Wood, R., C. S. Bretherton, D. Leon, A. D. Clarke, P. Zuidema, G. Allen, and H. Coe, 2011: An aircraft case study of the spatial transition from closed to open mesoscale cellular convection over the Southeast Pacific. *Atmos. Chem. Phys.*, **11**, 2341–2370, https://doi.org/10.5194/acp-11-2341-2011.

Yang, C., M. Diao, A. Gettelman, K. Zhang, J. Sun, G. McFarquhar, and W. Wu, 2021: Ice and supercooled liquid water distributions over the southern ocean based on in situ observations and climate model simulations. *J. Geophys. Res.*, **126**, e2021JD036 045, https://doi.org/10.1029/2021JD036045.

Young, G., and Coauthors, 2016: Observed microphysical changes in arctic mixed-phase clouds when transitioning from sea ice to open ocean. *Atmos. Chem. Phys.*, **16**, 13,945–13,967, https://doi.org/10.5194/acp-16-13945-2016.

Young, G. S., D. A. R. Kristovich, M. R. Hjelmfelt, and R. C. Foster, 2002: Rolls, streets, waves, and more: A review of quasi-two-dimensional structures in the atmospheric boundary layer. *Bull. Am. Meteor. Soc.*, **83**, 997 – 1002, https://doi.org/https://doi.org/10.1175/1520-0477(2002)083⟨0997:RSWAMA⟩2.3.CO;2.

Zaremba, T. J., R. M. Rauber, G. M. McFarquhar, P. J. DeMott, J. J. D'Alessandro, and W. Wu, 2021: Ice in southern ocean clouds with cloud top temperatures exceeding - 5 Celsius. *J. Geophys. Res.*, **126**, https://doi.org/10.1029/2021JD034574.

Zelinka, M., T. A. Myers, D. T. McCoy, S. Po-Chedley, P. M. Caldwell, and P. C. et al., 2020: Causes of higher climate sensitivity in CMIP6 models. *Geophys. Res. Lett.*, **47**, https://doi.org/10.1029/2019GL085782.

Zhao, X., and X. Liu, 2022: Primary and secondary ice production: interactions and their relative importance. *Atmos. Chem. Phys.*, **22**, 2585–2600, https://doi.org/10.5194/acp-22-2585-2022.

Zuidema, P., and K. F. Evans, 1998: On the validity of the independent pixel approximation for boundary layer clouds observed during ASTEX. *J. Geophys. Res.*, **103**, 6059–6074.

Zuidema, P., D. Painemal, S. deSzoeke, and C. Fairall, 2009: Stratocumulus cloud top height estimates and their climatic implications. *J. Clim.*, **22**, 4652–4666, https://doi.org/10.1175/2009JCLI2708.1.